Computational investigation of benzalacetophenone derivatives against SARS-CoV-2 as potential multi-target bioactive compounds

Pukar Khanal [a],[*],[1], Vishal S. Patil [b],[1], Vishwambhar V. Bhandare [b], Prarambh S.R. Dwivedi [a], C.S. Shastry [a], B.M. Patil [c], Shailendra S. Gurav [d], Darasaguppe R. Harish [b],[**], Subarna Roy [b]

[a] Department of Pharmacology, NGSM Institute of Pharmaceutical Sciences (NGSMIPS), Nitte (Deemed to be University), Mangalore, 575018, India
[b] ICMR-National Institute of Traditional Medicine, Belagavi, Karnataka, 590010, India
[c] PRES's Pravara Rural College of Pharmacy Pravaranagar, Loni, 413736, Maharashtra, India
[d] Department of Pharmacognosy and Phytochemistry, Goa College of Pharmacy, Panaji, Goa, India

A B S T R A C T

Benzalacetophenones, precursors of flavonoids are aromatic ketones and enones and possess the immunostimulant as well as antiviral activities. Thus, benzalacetophenones were screened against the COVID-19 that could be lethal in patients with compromised immunity. We considered ChEBI recorded benzalacetophenone derivative (s) and evaluated their activity against 3C-like protease (3CL^{pro}), papain-like protease (PL^{pro}), and spike protein of SARS-Cov-2 to elucidate their possible role as antiviral agents. The probable targets for each compound were retrieved from DIGEP-Pred at 0.5 pharmacological activity and all the modulated proteins were enriched to identify the probably regulated pathways, biological processes, cellular components, and molecular functions. In addition, molecular docking was performed using AutoDock 4 and the best-identified hits were subjected to all-atom molecular dynamics simulation and binding energy calculations using molecular mechanics Poisson-Boltzmann surface area (MMPBSA). The compound 4-hydroxycordoin showed the highest druglikeness score and regulated nine proteins of which five were down-regulated and four were upregulated. Similarly, enrichment analysis identified the modulation of multiple pathways concerned with the immune system as well as pathways related to infectious and non-infectious diseases. Likewise, 3'-(3-methyl-2-butenyl)-4'-O-β-ᴅ-glucopyranosyl-4,2'-dihydroxychalcone with 3CL^{pro}, 4-hydroxycordoin with PL^{pro} and mallotophilippen D with spike protein receptor-binding domain showed highest binding affinity, revealed stable interactions during the simulation, and scored binding free energy of −26.09 kcal/mol, −16.28 kcal/mol, and −39.2 kcal/mol, respectively. Predicted anti-SARS-CoV-2 activities of the benzalacetophenones reflected the requirement of wet lab studies to develop novel antiviral candidates.

1. Introduction

Coronaviruses are a group of ribonucleic acid (RNA) viruses that cause respiratory diseases in humans ranging from mild to lethal [1]. Since December 2019, COVID-19 arose as a pandemic throughout the world and infected millions of populations causing significant deaths. In addition, no vaccine so far has been developed to be 100% effective against COVID-19. Therefore multiple approaches were adopted for prophylaxis like social distancing, self-sanitation, proper use of masks, and immune booster consumption. Further, it was observed that the majority of deaths in this pandemic occurred among patients with compromised immunity [2]. This is vastly observed in the subjects with infectious and non-infectious diseases, often due to compromised immunity [3,4]. All these evidences suggest that the fraction of the population with compromised immunity is at higher risk for COVID-19 infection. In contrast, although attempts were made to develop new drugs or better vaccines, these exercises are costly and time-consuming. Of course, some approaches that had been attempted so far include repurposing existing drug molecules like chloroquine, remdesivir, and ivermectin [5]. However, further investigations are still required to

identify new molecules that are more effective with minimum side effects to avoid disease relapse as clinical reoccurrence of the COVID-19 symptoms is often reported after recovery.

Although single-target drug molecules are utilized to manage a broad series of diseases, they may not apply to the present scenario of COVID-19 management for two main reasons. First, the approved drug molecule for this pandemic is not available to target a specific macromolecule of a novel coronavirus. Hence, if the molecule against the protein (macromolecule) selected is less specific or ineffective dose potency at the supplied dose, it may cause the mutation of the target triggering further complications. Hence, it would be better in targeting the multiple proteins of the virus e.g. 3CL^{pro}, PL^{pro}, and spike protein, and inhibit the viral replication as they are chief mediators in viral multiplication inside the host cell. Additionally, an approach was made to spot the probable anti-viral molecules against coronavirus by targeting 3CL^{pro} which plays a chief role in the viral replication [6]. Further, PL^{pro} processes viral polyproteins to generate a functional replicase complex and enable viral spread [7]. In addition, spike protein binds to the angiotensin-converting enzyme 2 (ACE2) of the host cell and induces virus-cell membrane fusion [8]. Secondly, compromised immunity in subjects is one of the prime risk factors for coronavirus invasions [9] as it is a key to consider this facet in managing COVID-19 with immune boosters.

Benzalacetophenones (chalcones) are aromatic ketones and enones that are acknowledged for the central core to biotransform into biologically active compounds like flavonoids. These compounds can be obtained from medicinally important plant species of diverse families like Leguminosae, Asteraceae, and Moraceae [10]. Previously, benzalacetophenone derivatives were reported as the key players in immune system modification by manipulating the chemokines and inflammatory mediators [11]. In addition, they are also reported to regulate the dendritic cells, granulocytes, innate lymphoid cells, monocytes, macrophages, platelets, and T cells [11]. In addition, multiple reports on the anti-viral properties of benzalacetophenones and their derivatives are available [12–14].

Therefore, the present study aimed to investigate the dual action of benzalacetophenones *i.e.* immunomodulatory activity by identifying the multiple pathways that are concerned to attenuate the immune system and anti-viral potency against SARS-CoV-2 by targeting three proteins *i.e.* 3CL^{pro}, PL^{pro}, and spike protein.

2. Materials and methods

2.1. Retrieving bioactives and their targets

Benzalacetophenones were retrieved from Chemical Entities of Biological Interest (ChEBI; *https://www.ebi.ac.uk/chebi/*) and the protein-based targets were predicted from the DIGEP-Pred [15] web server (*http://www.way2drug.com/ge/*) by querying the simplified molecular-input line-entry system (SMILES) at the minimum pharmacological activity (Pa) > 0.5.

2.2. Prediction of drug-likeness and absorption, distribution, metabolism, excretion, and toxicity (ADMET) profile

The druglikeness of each compound was predicted based on the modified "*Lipinksi's Rule of Five*" [16] using MolSoft (*https://molsoft.com/mprop/*) based on molecular weight, *H*-bond donor and acceptor counts, and lipophilicity (MolLogP). Additionally, the ADMET profile of the top 5 hits of benzalacetophenones based on druglikeness scores was also examined using SwissADME [17] web server (*http://www.swissadme.ch/*) to investigate the physicochemical, lipophilicity, water-solubility, pharmacokinetics, druglikeness, and medicinal chemistry properties.

2.3. Enrichment analysis of regulated targets

The regulated (up/down-regulated) targets were queried in STRING [18] *ver.* 11.0 (*https://string-db.org/*) for *Homo sapiens*. Further, modulated proteins were enriched with reference to the Kyoto Encyclopedia of Genes and Genomes pathway database (KEGG; *https://www.genome.jp/kegg/pathway.html*) to identify the modulated pathways. In addition, the pathways related to the immune system were identified from published literature. The biological processes, molecular function, and cellular components were also identified through gene ontology (GO) analysis.

2.4. Network construction and analysis

The combined network of benzalacetophenones, regulated proteins, and modulated pathways was constructed using Cytoscape [19] *ver.* 3.5.1 (*https://cytoscape.org/*). The duplicate nodes/edges were removed during the network construction to avoid false hits. The whole network was then treated as directed before analysis. The final network was analyzed based on the edge count. In addition, the node size and color were set as "*low values to small size*" and "*low values to bright colors*" respectively.

2.5. Prediction of anti-viral spectra

Anti-viral spectra were traced by querying the SMILES of each compound in the prediction of activity spectra for substances [20] (PASS ONLINE; *http://www.way2drug.com/passonline/*) at Pa > pharmacological inactivity (Pi). Then, the probable anti-viral spectrum was identified using the keyword "*viral*". Records were queried for their probable pharmacological spectrum against multiple viruses like adenovirus, cytomegalovirus, hepatitis, herpes, human immunodeficiency viruses, influenza, parainfluenza, picornavirus, poxvirus, rhinovirus, and trachoma virus, and also as viral entry inhibitor.
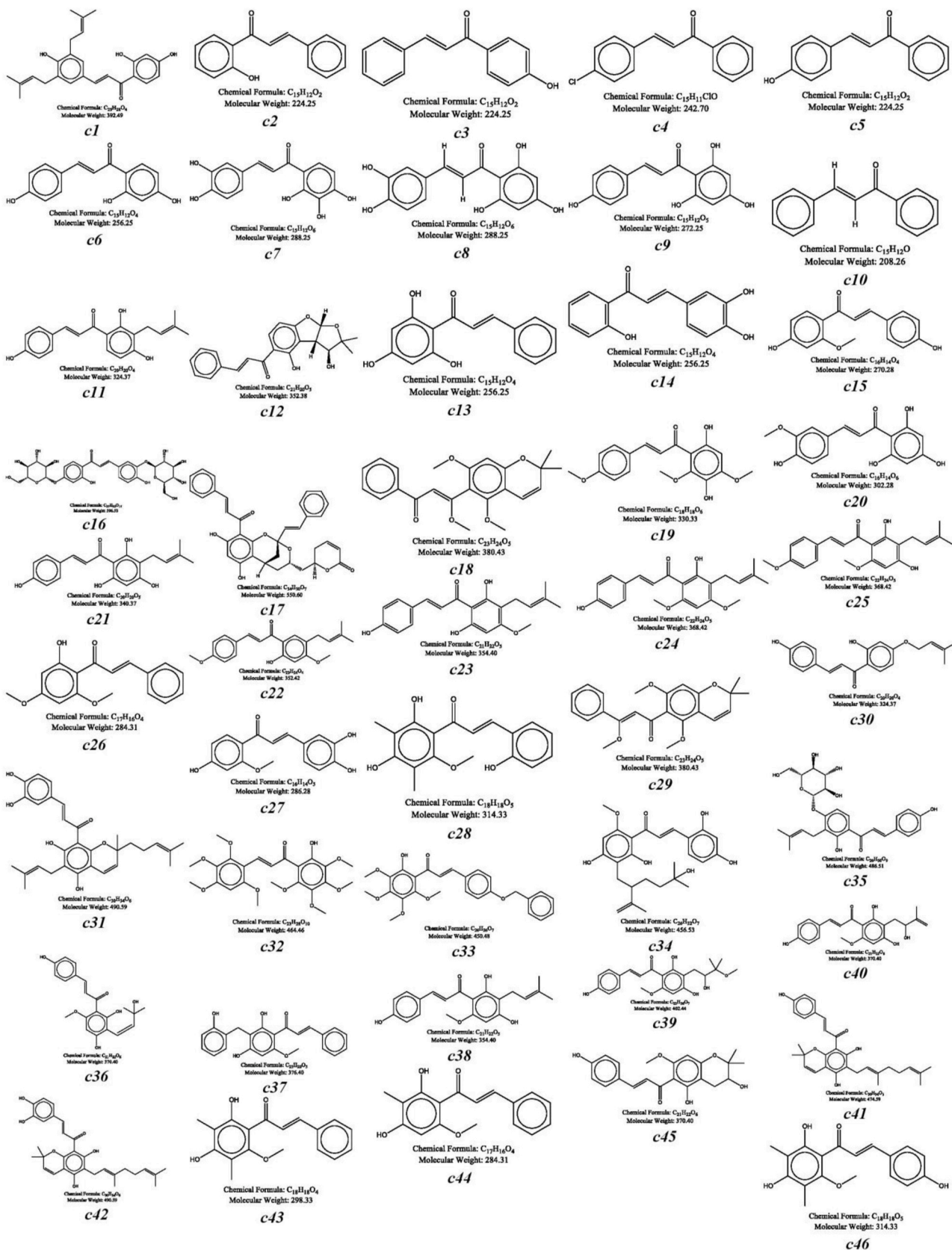
2.6. Molecular docking

Molecular docking was performed in three steps (a) ligand preparation, (b) preparation of macromolecule (target) and its active site determination, and (c) ligand-target docking.

Here, three-dimensional (3D) structures of selected small molecules and known molecules (standard) were retrieved from the PubChem small molecule database (*https://pubchem.ncbi.nlm.nih.gov/*) in the '*.sdf*' format. One of the molecules whose structure was not present in the PubChem database *i.e.* DRI-C23041 was generated using Marvin Sketch (*https://chemaxon.com/products/marvin*) *ver* 18.15. All the ligand structures were minimized using the '*uff*' forcefield [21] using the conjugate gradients algorithm. The ligands were converted into '*.pdbqt*' format by adding the gastigers charges and polar hydrogens.

The 3D structures for macromolecules 3CL^{pro} (PDB: 6LU7) and PL^{pro} (PDB: 4M0W) were retrieved from Research Collaboratory for Structural Bioinformatics (RCSB; *https://www.rcsb.org/*) structural database. The structure of the receptor-binding domain (RBD) of the omicron spike proteins (accession ID *P0DTC2)* was generated using homology modeling by employing "7T9J" as a template with SWISS-MODEL [22] web server (*https://swissmodel.expasy.org/*). Further, the active site of each target was determined using the computed atlas of surface topography of proteins (CASTp; *http://sts.bioe.uic.edu/castp/index.html?1bxw*) server and the ligand was docked within the predicted site.

Molecular docking was performed using AutoDock 4.0 [23] (*https://autodock.scripps.edu/*) to obtain ten docked poses per ligand. The intermolecular interaction compounds showing the least binding energy were selected to visualize protein-ligand interactions using BIOVIA Discovery Studio Visualizer 2019 [24] (*https://discover.3ds.com/discovery-studio-visualizer-download*).

Chemical Formula: C$_{20}$H$_{28}$O$_4$
Molecular Weight: 392.49
c1

Chemical Formula: C$_{15}$H$_{12}$O$_2$
Molecular Weight: 224.25
c2

Chemical Formula: C$_{15}$H$_{12}$O$_2$
Molecular Weight: 224.25
c3

Chemical Formula: C$_{15}$H$_{11}$ClO
Molecular Weight: 242.70
c4

Chemical Formula: C$_{15}$H$_{12}$O$_2$
Molecular Weight: 224.25
c5

Chemical Formula: C$_{15}$H$_{12}$O$_4$
Molecular Weight: 256.25
c6

Chemical Formula: C$_{15}$H$_{12}$O$_6$
Molecular Weight: 288.25
c7

Chemical Formula: C$_{15}$H$_{12}$O$_6$
Molecular Weight: 288.25
c8

Chemical Formula: C$_{15}$H$_{12}$O$_5$
Molecular Weight: 272.25
c9

Chemical Formula: C$_{15}$H$_{12}$O
Molecular Weight: 208.26
c10

Chemical Formula: C$_{20}$H$_{20}$O$_3$
Molecular Weight: 324.37
c11

Chemical Formula: C$_{21}$H$_{20}$O$_3$
Molecular Weight: 352.38
c12

Chemical Formula: C$_{15}$H$_{12}$O$_4$
Molecular Weight: 256.25
c13

Chemical Formula: C$_{15}$H$_{12}$O$_4$
Molecular Weight: 256.25
c14

Chemical Formula: C$_{16}$H$_{14}$O$_4$
Molecular Weight: 270.28
c15

Chemical Formula: C$_{20}$H$_{20}$O$_7$
Molecular Weight: 396.25
c16

Chemical Formula: C$_{34}$H$_{38}$O$_7$
Molecular Weight: 550.60
c17

Chemical Formula: C$_{23}$H$_{24}$O$_5$
Molecular Weight: 380.43
c18

Chemical Formula: C$_{18}$H$_{18}$O$_6$
Molecular Weight: 330.33
c19

Chemical Formula: C$_{18}$H$_{14}$O$_6$
Molecular Weight: 302.28
c20

Chemical Formula: C$_{20}$H$_{20}$O$_4$
Molecular Weight: 340.37
c21

Chemical Formula: C$_{22}$H$_{24}$O$_4$
Molecular Weight: 352.42
c22

Chemical Formula: C$_{21}$H$_{22}$O$_5$
Molecular Weight: 354.40
c23

Chemical Formula: C$_{23}$H$_{24}$O$_5$
Molecular Weight: 368.42
c24

Chemical Formula: C$_{23}$H$_{24}$O$_5$
Molecular Weight: 368.42
c25

Chemical Formula: C$_{17}$H$_{16}$O$_4$
Molecular Weight: 284.31
c26

Chemical Formula: C$_{16}$H$_{14}$O$_5$
Molecular Weight: 286.28
c27

Chemical Formula: C$_{18}$H$_{18}$O$_5$
Molecular Weight: 314.33
c28

Chemical Formula: C$_{23}$H$_{24}$O$_5$
Molecular Weight: 380.43
c29

Chemical Formula: C$_{20}$H$_{20}$O$_4$
Molecular Weight: 324.37
c30

Chemical Formula: C$_{28}$H$_{34}$O$_5$
Molecular Weight: 490.59
c31

Chemical Formula: C$_{23}$H$_{28}$O$_{10}$
Molecular Weight: 464.46
c32

Chemical Formula: C$_{26}$H$_{26}$O$_7$
Molecular Weight: 450.48
c33

Chemical Formula: C$_{26}$H$_{32}$O$_7$
Molecular Weight: 456.53
c34

Chemical Formula: C$_{29}$H$_{34}$O$_5$
Molecular Weight: 486.51
c35

Chemical Formula: C$_{22}$H$_{24}$O$_5$
Molecular Weight: 370.40
c36

Chemical Formula: C$_{23}$H$_{20}$O$_5$
Molecular Weight: 376.40
c37

Chemical Formula: C$_{21}$H$_{22}$O$_5$
Molecular Weight: 354.40
c38

Chemical Formula: C$_{26}$H$_{34}$O$_5$
Molecular Weight: 402.44
c39

Chemical Formula: C$_{23}$H$_{26}$O$_5$
Molecular Weight: 370.40
c40

Chemical Formula: C$_{29}$H$_{34}$O$_5$
Molecular Weight: 474.59
c41

Chemical Formula: C$_{30}$H$_{38}$O$_4$
Molecular Weight: 490.19
c42

Chemical Formula: C$_{18}$H$_{18}$O$_4$
Molecular Weight: 298.33
c43

Chemical Formula: C$_{17}$H$_{16}$O$_4$
Molecular Weight: 284.31
c44

Chemical Formula: C$_{23}$H$_{22}$O$_6$
Molecular Weight: 370.40
c45

Chemical Formula: C$_{18}$H$_{18}$O$_5$
Molecular Weight: 314.33
c46

(*caption on next page*)

Fig. 1. 2D-structures of benzalacetophenone derivatives retrieved from ChEBI database. *c1:* abyssinone VI; *c2:* 2′-hydroxychalcone; *C3:* 4′-hydroxychalcone; *c4:* 4-chlorochalcone; *c5:* 4-hydroxychalcone; *c6:* isoliquiritigenin; *c7:* okanin; *c8:* 2′,3,4,4′,6′-pentahydroxychalcone; *c9:* 2′,4,4′,6′-tetrahydroxychalcone; *c10:* chalcone; *c11:* isobavachalcone; *c12:* (+)-tephrosone; *c13:* pinocembrinchalcone; *c14:* 2′,3,4-trihydroxy-trans-chalcone; *c15:* 2′-O-methylisoliquiritigenin; *c16:* isobutrin; *c17:* obochalcolactone; *c18:* praecanson A; *c19:* 3′,6′-dihydroxy-2′,4,4′-trimethoxy-chalcone; *c20:* homoeriodictyolchalcone; *c21:* desmethylxanthohumol; *c22:* 4′-O-methylbavachalcone; *c23:* xanthogalenol; *c24:* 4′-O-methylxanthohumol; *c25:* 4-O-methylxanthohumol; *c26:* flavokawain B; *c27:* sappanchalcone; *c28:* 2,2′,4′-trihydroxy-6′-methoxy-3′,5′-dimethylchalcone; *c29:* 7-methoxypraecansone B; *c30:* 4-hydroxycordoin; *c31:* mallotophilippen E; *c32:* 1-(2-hydroxy-3,4,5,6-tetra-methoxyphenyl)-3-(2,3,4,6-tetramethoxyphenyl)-2-propen-1-one; *c33:* 4-benzyloxy-2′-hydroxy-3′,4′,5′,6′-tetramethoxychalcone; *c34:* kuraridinol; *c35:* 3′-(3-methyl-2-butenyl)-4′-O-β-ᴅ-glucopyranosyl-4,2′-dihydroxychalcone; *c36:* candidachalcone; *c37:* 2′,4′-dihydroxy-3′-(2-hydroxy benzyl)-6′-methoxy chalcone; *c38:* xanthohumol; *c39:* oxygenated xanthohumol; *c40:* xanthohumol D; *c41:* mallotophilippen C; *c42:* mallotophilippen D; *c43:* 2′,4′-dihydroxy-6′-methoxy-3′,5′-dimethylchalcone; *c44:* 2′,4′-dihydroxy-3′-methyl-6′-methoxychalcone; *c45:* xanthohumol B; and *c46:* (E)-4,2′,4′-trihydroxy-6′-methoxy-3′,5′-dimethylchalcone.

2.7. Stability of the docked complexes

The best-docked conformations from the three different targets were selected and subjected to all-atom molecular dynamics (MD) simulation for 150 ns in explicit solvent to investigate their structural stabilities and intermolecular interactions. We used GROMACS (*https://www.gromacs.org/*) 2021.3 software package to perform MD simulations with the Amber ff99SB-ildn force field [25,26]. The partial charges of the small molecules were generated by performing quantum calculation using an antechamber with a '*bcc*' charge model and topology parameters of the ligands and whole complex were generated using the xleap module of AmberTools (https://ambermd.org/AmberTools.php). The prepared systems were solvated using a three-site water (TIP3P) model in a rectangular box having 10.0 Å boundary conditions from the protein's edges in all directions. The charges on the prepared systems were neutralized by adding the required number of counter ions. Steepest descent followed by conjugate gradient energy minimization method was used to obtain near-global state least energy conformations. The systems were equilibrated using "canonical (NVT) and isobaric (NPT)" ensembles for 1 ns. In NVT equilibration, a modified Berendsen thermostat algorithm was applied to maintain the constant volume and temperature (300 K). In NPT equilibration, Parrinello-Rahman barostat was applied to maintain the constant pressure of 1 bar. In addition, to compute coulomb, van der Waals, and the long-range electrostatic interactions, the Particle Mesh Ewald approximation was applied with a cut-off value of 1 nm. Similarly, the LINear Constraint Solver algorithm was used to constraint bond length. All the complexes were subjected to a production run of 150 ns and the coordinates were recorded at every 2 fs. However, the spike protein-mallotophilippen D (*c42*) complex was subjected to 200 ns of simulation as this complex reached an equilibrium state after 150 ns. The trajectories generated were analyzed using in-build gromacs utilities, and some other additional software packages were used for specific analysis wherever required.

2.8. Investigation of binding affinity using molecular mechanics Poisson–Boltzmann surface area (MM-PBSA)

The relative binding energy of a ligand-protein complex was used in MD simulations and thermodynamic computations to explore the binding affinities. In the present work, the '*g_mmpbsa*' tool [26] was used to calculate the relative binding energy and its contribution to single residues using the MM-PBSA approach [27]. The parameters used to calculate the binding energy were considered from earlier studies [28, 29]. The binding energy was calculated over the stable trajectory observed between 100 and 150 ns using 50 representative snapshots.

2.9. Analysis of principal component and dynamic cross-correlation matrix

Principal component analysis (PCA) examines the key types of molecular motion using MD trajectories [29–31]. This involves removing the molecule's translational and rotational motion using the "*least square fit*" to the reference structure. A covariance matrix was generated by a linear transform of cartesian coordinate space and is diagonalized to produce a group of eigenvectors that reflect the direction of the molecule's motion. The eigenvalue related to each eigenvector indicates the energy contribution of that part to the motion. The projection of the trajectory on a specific eigenvector illustrates the '*time-dependent movements*' that the components perform in a specific vibrational mode. The projection's time average reveals the contribution of atomic vibration components to this mode of coordinated motion. The eigenvectors and eigenvalues of the trajectory were generated using the gromacs in-built utilities "*g_covar*" by calculating and diagonalizing the covariance matrix. In addition, the "*g_anaeig*" tool was used to analyze and illustrate the eigenvectors [29–32].

The dynamic cross-correlation matrix (DCCM) evaluates the magnitude of all pairwise cross-correlation coefficients to identify correlated (positive or negative) motion among pairs of atoms [33]. In this section, we studied each element of DCCM, where $C_{ij} = 1$ indicates the same period and phase (positively correlated), $C_{ij} = 0$ indicates no correlation and $C_{ij} = -1$ indicates that the fluctuations of i and j are negatively correlated [33].

3. Results

3.1. Retrieving bioactives and their targets

A total of 46 benzalacetophenones (Fig. 1) were retrieved from ChEBI in which 4-hydroxychalcone (*c5*) regulated the maximum number of proteins. In addition, *CASP8* was majorly targeted by utmost benzalacetophenones derivatives.

3.2. Calculation of druglikeness and ADMET profile

Herein, 4-hydroxycordoin (*c30*) possessed the highest druglikeness score *i.e.* 0.8 with the 324.14 molecular weight, 4 *H*-bond acceptors, 2 *H*-bond donors, and 5.13 MolLogP (Table 1). In addition, oxygenated xanthohumol (*c39*), abyssinoneVI (*c1*), isobavachalcone (*c11*), and mallotophilippen E (*c31*) also scored the positive drug-likeness *i.e.* 0.79, 0.71, 0.6, and 0.6 respectively. Further, all the top 5 hit benzalacetophenones followed Lipinksi's Rule of Five and Veber's rule without violating any rule. However, molecules violated the Ghose, Egan, and Muegge rule. Similarly, molecules were predicted as various CYP450 isoenzymes (*CYP1A2, CYP2C19, CYP2C9, CYP2D6,* and *CYP3A4*) inhibitors. Further, mallotophilippen E (*c31*) showed low gastrointestinal absorbability. The detailed physicochemical profile of hit benzalacetophenones including their lipophilicity, water-solubility, pharmacokinetics, and druglikeness properties are presented in Fig. 2.

3.3. Enrichment and network analysis

A total of 55 pathways were modulated by the combined action of queried benzalacetophenones. Among them, the fluid shear stress and atherosclerosis were majorly modulated through 9 proteins *i.e. CCL2, CTNNB1, CYBA, HMOX1, MMP2, NFE2L2, NQO1, PLAT,* and *TNFRSF1A* against 133 background proteins with the lowest false discovery rate *i.e.* 1.73E-09. However, 12 proteins (*AR, CASP8, CCND2, CTNNB1, HMOX1, KLK3, MDM2, MMP2, NFE2L2, NOS2, NQO1,* and *RARA*) within pathways in cancer were regulated against 515 background proteins (Table 2, detailed in supplementary file; sheet S1). Similarly, the

Table 1

Druglikeness score of Benzalacetophenone derivatives.

Compounds	MF	MW	NHBA	NHBD	MolLogP	MolPSA(A²)	MolVol (A³)	BBB Score	DLS
c1	$C_{25}H_{28}O_4$	392.2	4	3	6.98	62.86	456.87	3.6	0.71
c2	$C_{15}H_{12}O_2$	224.08	2	1	4.09	29.76	231.36	4.95	-0.25
c3	$C_{15}H_{12}O_2$	224.08	2	1	3.2	30.83	230.73	4.94	-0.38
c4	$C_{15}H_{11}ClO$	242.05	1	0	4.24	13.21	237.37	5.09	-1
c5	$C_{15}H_{12}O_2$	224.08	2	1	3.08	30.83	230.73	4.94	-0.51
c6	$C_{15}H_{12}O_4$	256.07	4	3	2.91	65	252.53	3.09	0.34
c7	$C_{15}H_{12}O_6$	288.06	6	5	2.12	93.82	275.83	2.68	0.23
c8	$C_{15}H_{12}O_6$	288.06	6	5	2.31	97.02	278.64	2.64	-0.06
c9	$C_{15}H_{12}O_5$	272.07	5	4	2.7	81.54	265.92	2.86	-0.23
c10	$C_{15}H_{12}O$	208.09	1	0	3.65	13.21	220.18	5.12	-1.23
c11	$C_{20}H_{20}O_4$	324.14	4	3	4.92	62.86	356.64	3.53	0.6
c12	$C_{21}H_{20}O_5$	352.13	5	2	3.51	60.37	365.3	3.61	-0.19
c13	$C_{15}H_{12}O_4$	256.07	4	3	3.26	63.93	255.37	3.11	-0.78
c14	$C_{15}H_{12}O_4$	256.07	4	3	3.13	62.86	254.63	3.12	0.3
c15	$C_{16}H_{14}O_4$	270.09	4	2	2.83	56.08	272.53	3.78	0.11
c16	$C_{27}H_{32}O_{15}$	596.17	15	10	-1.66	206.11	527.34	1.24	0.58
c17	$C_{34}H_{30}O_7$	550.2	7	2	6.65	79.74	593.19	1.85	0.18
c18	$C_{23}H_{24}O_5$	380.16	5	0	4.49	41.75	419.93	4.47	-0.59
c19	$C_{18}H_{18}O_6$	330.11	6	2	3.12	68.13	338.96	3	0.15
c20	$C_{16}H_{14}O_6$	302.08	6	4	2.65	88.11	298.64	2.75	-0.04
c21	$C_{20}H_{20}O_5$	340.13	5	4	4.79	79.41	370.03	2.81	0.4
c22	$C_{22}H_{24}O_4$	352.17	4	1	5.97	44.94	397.02	4.43	0.2
c23	$C_{21}H_{22}O_5$	354.15	5	3	5.24	70.49	390.03	2.91	0.58
c24	$C_{22}H_{24}O_5$	368.16	5	2	5.39	61.57	410.03	3.62	0.51
c25	$C_{22}H_{24}O_5$	368.16	5	2	5.4	60.42	411.32	3.63	0.51
c26	$C_{17}H_{16}O_4$	284.1	4	1	3.85	44.94	296.67	4.34	-0.33
c27	$C_{16}H_{14}O_5$	286.08	5	3	2.44	71.56	285.25	3	0.44
c28	$C_{18}H_{18}O_5$	314.12	5	3	4.71	68.44	328.92	3.01	-0.68
c29	$C_{23}H_{24}O_5$	380.16	5	0	4.95	41.75	419.93	4.47	-0.54
c30	$C_{20}H_{20}O_4$	324.14	4	2	5.13	54.8	354.51	3.96	0.8
c31	$C_{30}H_{34}O_6$	490.24	6	4	8.17	83.48	569.89	2.31	0.6
c32	$C_{23}H_{28}O_{10}$	464.17	10	1	3.75	90.26	486.52	2.35	-0.26
c33	$C_{26}H_{26}O_7$	450.17	7	1	5.15	66.79	464.12	2.95	-0.78
c34	$C_{26}H_{32}O_7$	456.21	7	5	5.23	103.22	498.68	2.17	0.51
c35	$C_{26}H_{30}O_9$	486.19	9	6	2.72	126.25	487.03	1.52	0.51
c36	$C_{21}H_{22}O_6$	370.14	6	4	3.74	86.68	408.4	2.65	0.27
c37	$C_{23}H_{20}O_5$	376.13	5	3	4.93	69.15	380.27	2.55	0.59
c38	$C_{21}H_{22}O_5$	354.15	5	3	4.87	70.49	390.03	2.91	0.58
c39	$C_{22}H_{26}O_7$	402.17	7	4	3.48	93.38	422.93	2.48	0.79
c40	$C_{21}H_{22}O_6$	370.14	6	4	3.99	86.64	389.47	2.65	0.53
c41	$C_{30}H_{34}O_5$	474.24	5	3	8.72	67.81	561.92	3.21	0.02
c42	$C_{30}H_{34}O_6$	490.24	6	4	8.34	83.29	574.64	2.32	0.45
c43	$C_{18}H_{18}O_4$	298.12	4	2	5	51.89	318.39	3.94	-0.97
c44	$C_{17}H_{16}O_4$	284.1	4	2	3.89	52.87	297.32	3.88	-0.15
c45	$C_{21}H_{22}O_6$	370.14	6	3	3.69	76.5	392.02	2.79	0.42
c46	$C_{18}H_{18}O_5$	314.12	5	3	4.43	69.51	328.94	3	-0.5

c1: abyssinone VI, *c2:* 2'-hydroxychalcone, *c3:* 4'-hydroxychalcone, *c4:* 4-chlorochalcone, *c5:* 4-hydroxychalcone, *c6:* isoliquiritigenin, *c7:* okanin, *c8:* 2',3,4,4',6'-pentahydroxychalcone, *c9:* 2',4,4',6'-tetrahydroxychalcone, *c10:* chalcone, *c11:* isobavachalcone, *c12:* (+)-tephrosone, *c13:* pinocembrinchalcone, *c14:* 2',3,4-trihydroxy-trans-chalcone, *c15:* 2'-O-methylisoliquiritigenin, *c16:* isobutrin, *c17:* obochalcolactone, *c18:* praecanson A, *c19:* 3',6-dihydroxy-2',4,4'-trimethoxy-chalcone, *c20:* homoeriodictyolchalcone, *c21:* desmethylxanthohumol, *c22:* 4'-O-methylbavachalcone, *c23:* xanthogalenol, *c24:* 4'-O-methylxanthohumol, *c25:* 4-O-methylxanthohumol, *c26:* flavokawain B, *c27:* sappanchalcone, *c28:* 2,2',4'-trihydroxy-6'-methoxy-3',5'-dimethylchalcone, *c29:* 7-methoxypraecansone B, *c30:* 4-hydroxycordoin, *c31:* mallotophilippen E, *c32:* 1-(2-hydroxy-3,4,5,6-tetramethoxyphenyl)-3-(2,3,4,6-tetramethoxyphenyl)-2-propen-1-one, *c33:* 4-benzyloxy-2'-hydroxy-3',4',5',6'-tetramethoxychalcone, *c34:* kuraridinol, *c35:* 3'-(3-methyl-2-butenyl)-4'-O-beta-D-glucopyranosyl-4,2'-dihydroxychalcone, *c36:* candidachalcone, *c37:* 2',4'-dihydroxy-3'-(2-hydroxy benzyl)-6'-methoxy chalcone, *c38:* xanthohumol, *c39:* oxygenated xanthohumol, *c40:* xanthohumol D, *c41:* mallotophilippen C, *c42:* mallotophilippen D, *c43:* 2',4'-dihydroxy-6'-methoxy-3',5'-dimethylchalcone, *c44:* 2',4'-dihydroxy-3'-methyl-6'-methoxychalcone, *c45:* xanthohumol B, and *c46:* (E)-4,2',4'-trihydroxy-6'-methoxy-3',5'-dimethylchalcone. **MF:** Molecular formula, **MW:** Molecular weight, **NHBA:** Number of H-bond acceptor, **NHBD:** Number of H-bond donor, **BBB:** Blood brain barrier, **DLS:** Druglikeness score.
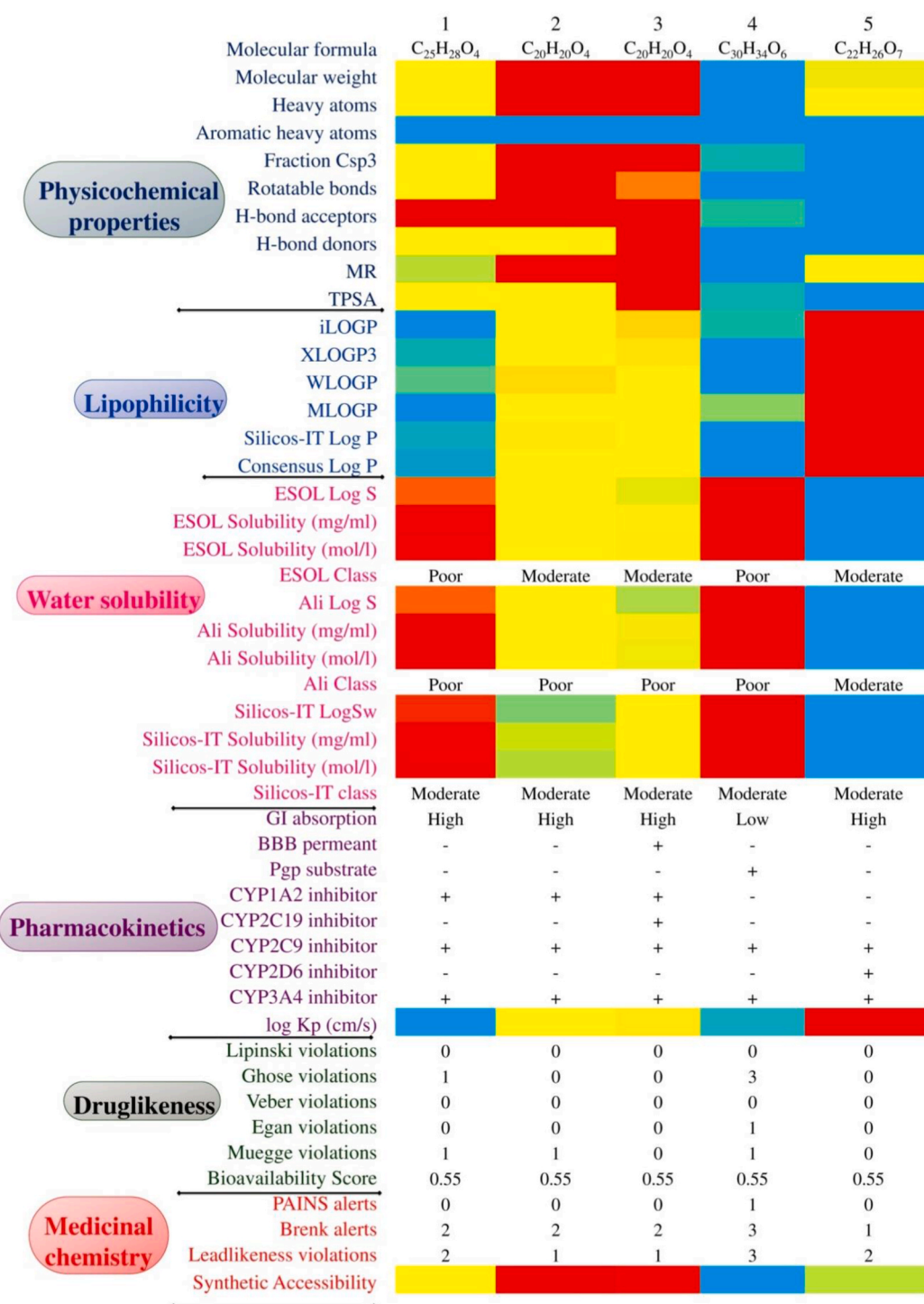
Color map   Low   Medium   High

Fig. 2. ADMET profile of five lead hit benzalacetophenone derivatives with positive druglikeness score. (1) abyssinone VI, (2) isobavachalcone, (3) 4-hydroxycordoin, (4) mallotophilippen E, and (5) oxygenated xanthohumol
Color scale Red: Low, Yellow: Medium, Blue: High.

network interaction identified *CASP8* protein to be majorly regulated. The protein-protein interaction of the benzalacetophenone(s)-regulated proteins based on curated databases, experimentally determined, gene neighborhood, gene fusions, gene co-occurrence, text mining, co-expression, and protein homology is presented in Fig. 3. Further, the benzalacetophenones' interaction with their targets and regulated pathways concerning the KEGG database is presented in Fig. 4. Similarly, a total of 53 molecular functions GO terms were detected in which steroid hormone receptor activity; GO:*0003707* was identified to

modulate 6 genes *i.e. AR*, *NR3C1*, *PGR*, *PPARA*, *RARA*, and *VDR* against 59 background genes at the lowest false discovery rate *i.e.* 5.71E-07 (Table 3; detailed in supplementary file; sheet S2). In addition, a total of 33 cellular components GO terms were detected in which 14 genes were modulated from the extracellular space *i.e. CCL2*, *CD86*, *FLT1*, *HBA1*, *HMOX1*, *KLK3*, *MMP2*, *MMP7*, *NPPB*, *PLAT*, *PLAU*, *PROC*, *TIMP1*, and *TNFRSF1A* against 1134 background genes at 1.12E-05 false discovery rate (Table 4; detailed in supplementary file; sheet S3). Further, a total of 521 biological processes GO terms were identified in which

Table 2

Benzalacetophenone derivatives-regulated top 10 KEGG pathways.

Term description [Term ID]	Observed gene count	Background gene count	False discovery rate	Matching proteins in the network
Fluid shear stress and atherosclerosis [hsa05418]	9	133	1.73E-09	*CCL2, CTNNB1, CYBA, HMOX1, MMP2, NFE2L2, NQO1, PLAT, TNFRSF1A*
Pathways in cancer [hsa05200]	12	515	3.46E-08	*AR, CASP8, CCND2, CTNNB1, HMOX1, KLK3, MDM2, MMP2, NFE2L2, NOS2, NQO1, RARA*
Transcriptional misregulation in cancer [hsa05202]	8	169	1.32E-07	*CCND2, CD14, CD86, FLT1, MDM2, PLAT, PLAU, RARA*
HIF-1 signaling pathway [hsa04066]	6	98	2.49E-06	*FLT1, GAPDH, HMOX1, NOS2, TFRC, TIMP1*
Prostate cancer [hsa05215]	6	97	2.49E-06	*AR, CTNNB1, KLK3, MDM2, PLAT, PLAU*
p53 signaling pathway [hsa04115]	4	68	0.00036	*CASP8, CCND2, CHEK1, MDM2*
Tuberculosis [hsa05152]	5	172	0.00066	*CASP8, CD14, NOS2, TNFRSF1A, VDR*
Chagas disease (American trypanosomiasis) [hsa05142]	4	101	0.0012	*CASP8, CCL2, NOS2, TNFRSF1A*
Ferroptosis [hsa04216]	3	40	0.0016	*GSS, HMOX1, TFRC*
MicroRNAs in cancer [hsa05206]	4	149	0.0041	*CCND2, HMOX1, MDM2, PLAU*

Color map | Low | Medium | High

The enrichment KEGG pathways analysis was based on the whole genome (*Homo sapiens*) statistical background.

response to a stimulus; GO:*0050896* was identified to regulate 40 genes *i.e. AR, CASP8, CAT, CCL2, CCND2, CD14, CD83, CD86, CHEK1, CTNNB1, CYBA, CYP3A4, FLT1, GAPDH, GSS, HBA1, HMOX1, KLK3, KRT1, KRT8, MDM2, MMP2, MMP7, NFE2L2, NOS2, NPPB, NQO1, NR3C1, PGR, PLAT, PLAU, PPARA, PRDX1, PROC, RARA, TFRC, TIMP1, TNFRSF1A, TOP2A*, and *VDR* against 7824 genes at 5.09E-12 false discovery rate (Table 5; detailed in supplementary file; sheet S4); top 5 hits of GO analysis for cellular components, biological process, and molecular function are presented in Fig. 5. Similarly, the plot was analyzed for neighborhood connectivity (y = 28.402–0.324x, ρ (X,Y) = 0.638), between centrality (y = 0.001x$^{0.28}$, ρ (X,Y) = 1), closeness centrality (y = 0.92x$^{0.013}$, ρ (X,Y) = 0.02), in degree distribution (y = 8.364–0.208x, ρ (X,Y) = 0.271) and out-degree distribution (y = 15.397–0.813x, ρ (X,Y) = 0.641); represented in Fig. 6.

3.4. Prediction of anti-viral spectra of benzalacetophenones

A total of 17 anti-viral spectra were identified in which maximum activity was against herpes virus *i.e.* 12.57% and the minimum was for parainfluenza *i.e.* 0.57%. The detailed anti-viral spectra of the benzalacetophenones are represented in Fig. 7.

3.5. Homology modeling for RBD the domain of spike protein

The homology model of spike protein was generated using the SWISS-MODEL server and validated for its overall quality mode using the Global Model Quality Estimate (GMQE) which was 0.83. The GMQE value ranges from 0 to 1 and it reflects the expected accuracy of the model with respect to the template. In addition, the ERRAT score (89.86%) revealed the overall quality of the generated model. Further, the stereochemical properties were analyzed using the Ramachandran plot which showed the presence of all residues in the most favored and additionally allowed region.

3.6. Molecular docking

Among all the benzalacetophenones derivatives, 4-hydroxycordoin (**c30**), 3'-(3-methyl-2-butenyl)-4'-O-β-D-glucopyranosyl-4,2'-dihydroxychalcone (**c35**), and mallotophilippen D (**c42**) scored the least binding energy with 3CL^{pro}, PL^{pro}, and omicron spike protein RBD respectively. The estimated binding energy from the docking study for 3CL^{pro}- 3'-(3-methyl-2-butenyl)-4'-O-β-D-glucopyranosyl-4,2'-dihydroxychalcone

(**c35**), PL^{pro}-4-hydroxycordoin (**c30**) and spike protein-mallotophilippenD (**c42**) was −8.4, −8.2, and −7.9 kcal/mol respectively. The detailed binding mode and their intermolecular interactions are presented in Fig. 8 (detailed in supplementary file sheet S5). Similarly, obochalcolactone (**c17**) showed the highest binding affinity (−8.5 kcal/mol) with 3CL^{pro} but had no *H*-bond interaction. However, 3'-(3-methyl-2-butenyl)-4'-O-β-D-glucopyranosyl-4,2'-dihydroxychalcone (**c35**) possessed the 2 *H*-bond interactions with *Ser144* and *Cys145* and scored the least binding energy (−8.4 kcal/mol). A standard molecule *i. e.* carmofur showed the binding energy of −5.9 kcal/mol *via* 7 *H*-bond interactions with key conserved residues namely *Leu141, Gly143, Ser144* (2), *Cys145, His163*, and *Glu166*. In addition, compound 4-hydroxycordoin (**c30**) and xanthohumol (**c38**) showed the highest binding affinity (binding energy −8.2 kcal/mol) with protein PL^{pro} and formed stable *H*-bond interactions (1 and 2 *H*-bonds respectively). Further, isobutrin (**c16**) had the highest *H*-bond interactions *i.e.* 8 by interacting with *Val203, Ala177, Thr75, Asn157, Tyr155, His176*, and *Asp77*. In addition, a standard molecule GRL0617 scored the binding energy of −7.4 kcal/mol *via* 2 *H*-bonds with *Tyr265* and *Gly164* and 5 hydrophobic interactions with *Asp165, Tyr269* (2), *Lys158, Tyr265*, and *Leu163*. Likewise, mallotophilippenD (**c42**) showed the highest binding affinity (binding energy −7.9 kcal/mol) with spike protein and formed 2 *H*-bond interactions with *Asn437*, and *Lys440* and 11 hydrophobic interactions with *Leu441, Lys440, Pro373, Phe374, Phe342*, and *Leu368*. A standard molecule DRI-C23041 showed the binding energy of −9.4 kcal/mol *via* 2 H-bonds with *Lys440* and *Asp364* and by forming 5 hydrophobic interactions with *Leu441, Lys440* (2), *Val367*, and *Asp339*. It was interesting to note that all the best-identified compounds showed stable and conserved intermolecular interactions.

3.7. Stability of the docked complexes

3.7.1. Stability of 3CL^{pro}-3'-(3-methyl-2-butenyl)-4'-O-β-D-glucopyranosyl-4,2'-dihydroxychalcone (c35) complex

The all-atom explicit MD simulation trajectory revealed stable dynamics during 150 ns after the 50 ns equilibration period. The average root mean square deviation (RMSD) value for backbone and complex was observed to be ∼2 Å and ∼2.5 Å, respectively. The loop formed between residues *Leu177* to *Ile200* located adjacent to the binding site (connecting to β-sheet and helice) showed minimal residual fluctuations up to 1.6 Å. The C-terminal region comprising flexible loops was highly dynamic and expressed root-mean-square fluctuation value > 3 Å due to
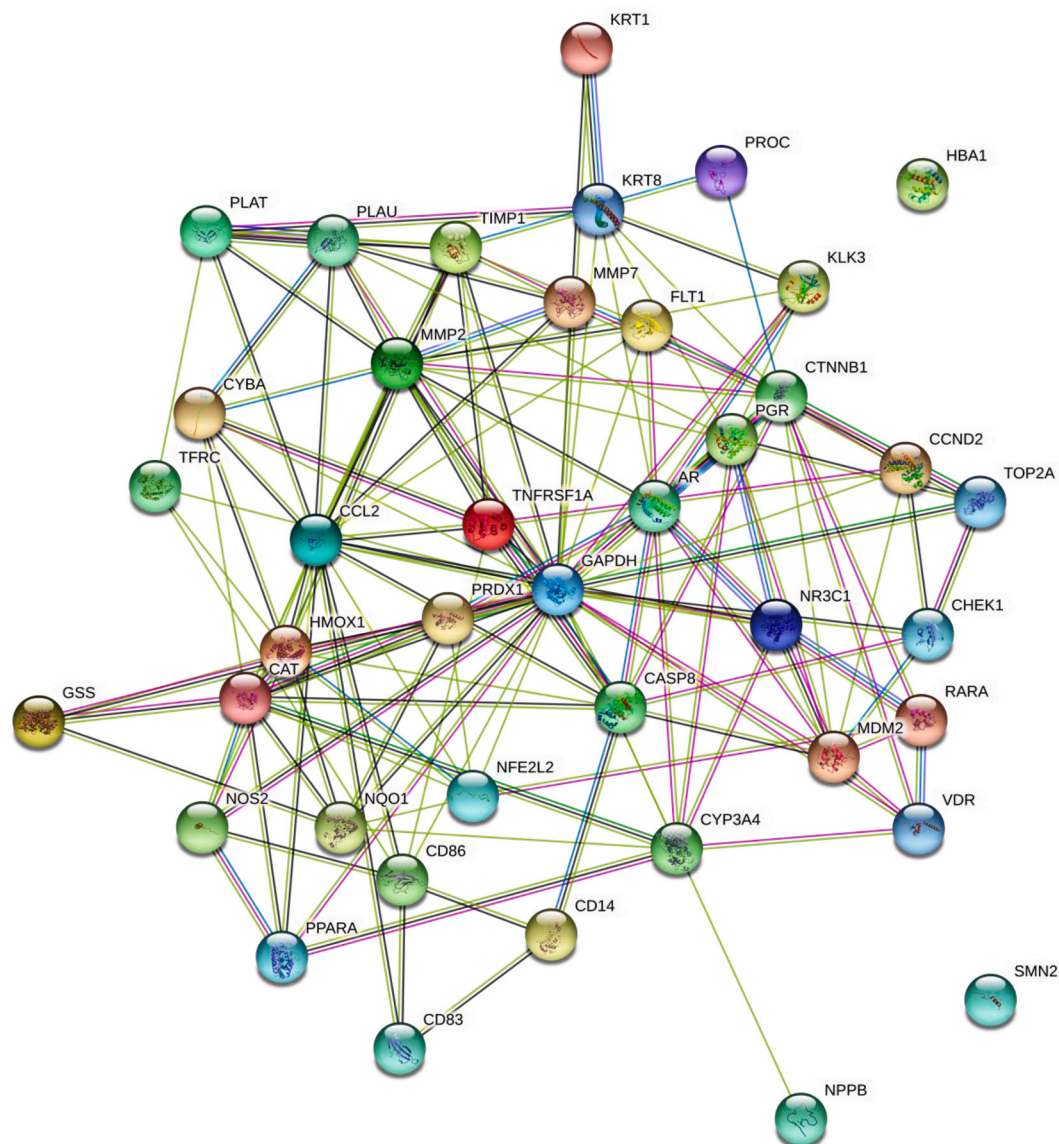
**Fig. 3.** Protein-protein interaction of the benzalacetophenone(s)-regulated targets. Node color; **colored nodes**: query proteins and first shell of interactors, **white nodes**: second shell of interactors, Node content; **empty nodes**: proteins of unknown 3D structure, **filled nodes**: some 3D structure is known or predicted, **Known Interactions**; *from curated databases,* *experimentally determined,* **Predicted Interactions**; *gene neighborhood,* *gene fusions,* *gene co-occurrence&*;**Others**; *textmining,* *co-expression,* *protein homology.*

their flexible nature. It was interesting to note that the residues actively participated in the stable and conserved non-bonded interactions; showed much lesser fluctuations. In addition, the radius of gyration (Rg) explains the structural folding and compactness of the molecule. The Rg value revealed stable folding during the simulation and revealed stable complex formation (Fig. 9). The solvent-accessible surface area (SASA) was analyzed to distinguish the protein compactness behavior. The initial and final average surface area occupied by 3CL^{pro} and 3'-(3-methyl-2-butenyl)-4'-O-β-D-glucopyranosyl-4,2'-dihydroxychalcone (**c35**) docked complex was 149.89 nm^2 and 147.53 nm^2 respectively. The average surface area occupied by the complex was 148 nm^2. The supplementary movie (S1) represents the detailed binding mode of 3'-(3-methyl-2-butenyl)-4'-O-β-D-glucopyranosyl-4,2'-dihydroxychalcone

(**c35**) with 3CL^{pro}. This complex formed 11 stable *H*-bonds of which 7 were consistent throughout the simulations. It was assumed that the stable complex formation was mainly promoted by stable *H*-bond interactions.

Supplementary video related to this article can be found at https://doi.org/10.1016/j.compbiomed.2022.105668.

Further, the binding affinity of the complex was investigated using the MMPBSA approach by the g_mmpbsa tool. Table 6 summarizes the free energy contribution of lead hits and standard molecules with their respective targets. The estimated relative binding energy of the complex 3CL^{pro}-3'-(3-methyl-2-butenyl)-4'-O-β-D-glucopyranosyl-4,2'-dihydroxychalcone (**c35**) complex was −26.09 kcal/mol. Further, the residues contributing most to the binding energy were identified by calculating
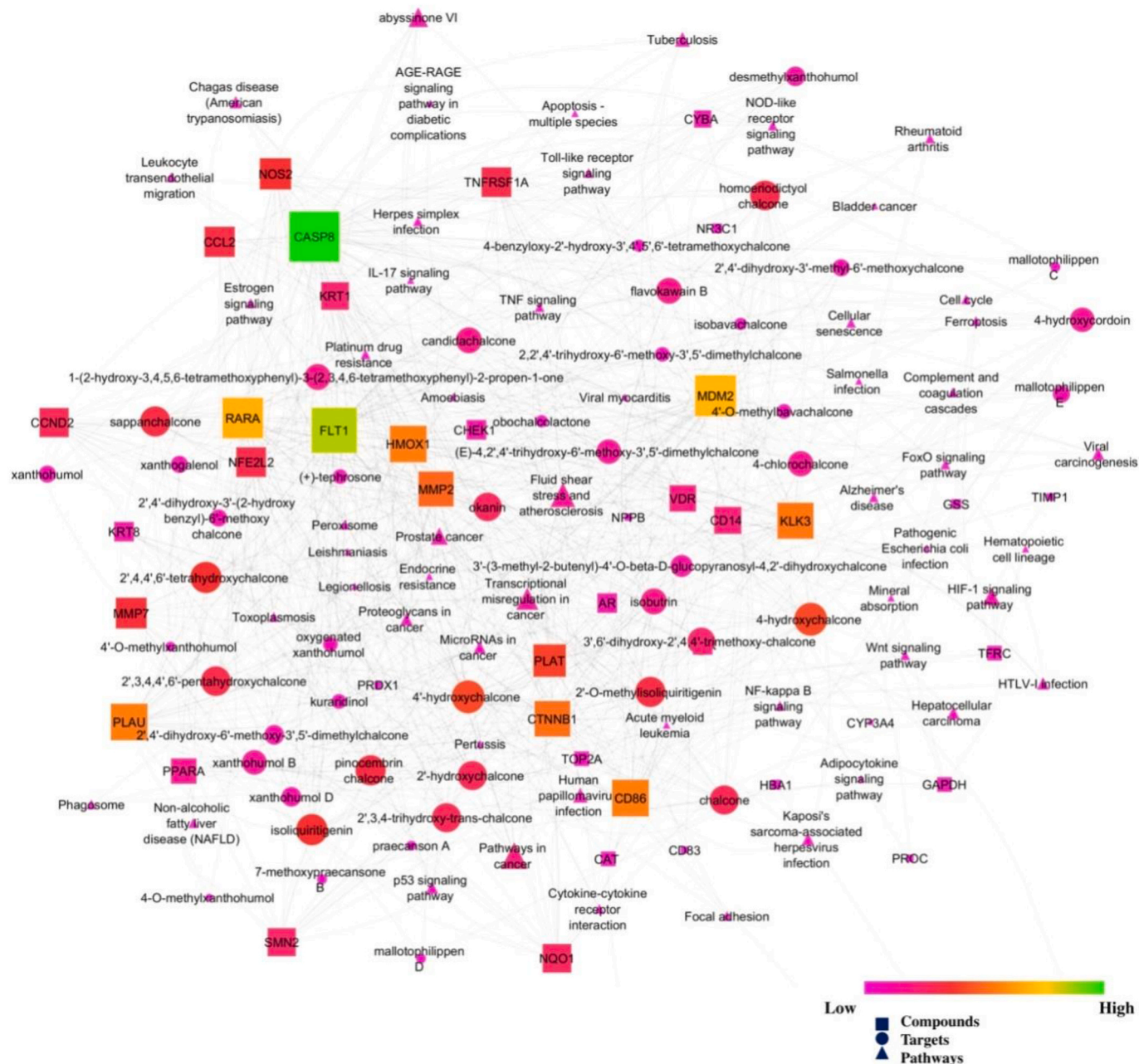
Fig. 4. Network interaction of benzalacetophenone derivatives with their targets and regulated pathways concerning the KEGG database. In the network interaction, circle, square, and triangle represent benzalacetophenone, proteins, and pathways respectively. The node with lower edge count is represented by pink which gradually increase to green presenting the node with maximum edge count.

residue decomposition energy. The residues *Thr25, Met49, Phe140, Asn142, Gly143, Ser144, Cys145, His163, Met165,* and *Asp187* favored the stable complex formation. However, *Glu166* residue did not favor the interactions. Among these residues, *Cys145* showed significant contributions to the binding energy as it had the least contribution energy (−4.42 kJ/mol). However, other residues also possessed the contribution energy between −2.62 to −3.99 kJ/mol and participated in stable complex formation.

3.7.2. Stability of 3CL^pro-carmofur complex

The complex 3CL^pro-carmofur showed stable dynamics during the 150 ns of simulation after an equilibration period (60 ns). The average RMSD value for backbone and complex was 2.34 Å and 2.81 Å, respectively. The N and C- terminal residues showed maximum residual fluctuations (~10 Å). However, the residues engaged in the stable and conserved non-bonded interactions showed relatively much lesser fluctuations (~2.0 Å). The Rg value revealed a folding pattern during ~30 ns (Fig. 10) and was found to express partial unfolding indicating the stable ligand binding. In addition, it was observed that the initial and final average surface area occupied by 3CL^pro and carmofur docked complex was 145.97 nm^2 and 148.49 nm^2 respectively. The average hydrophobic surface area occupied by the complex was 148.32 nm^2 which represented a protein unfolding and flexibility of the binding pocket. The supplementary movie (S2) represents the detailed binding mode and stable dynamics of carmofur to 3CL^pro. This complex formed 6 stable *H*-bonds of which 4 were consistent throughout the simulations. It was believed that these stable *H*-bond interactions promoted the stable complex formation. The estimated relative binding energy of the complex 3CL^pro-carmofur complex was −16.67 kcal/mol. Further, the major residues contributing to the binding energy were identified by

Table 3

Benzalacetophenone derivatives-regulated top 10 molecular functions.

Term description [Term ID]	Observed gene count	Background gene count	False discovery rate	Matching proteins in the network
steroid hormone receptor activity [GO:0003707]	6	59	5.71E-07	AR, NR3C1, PGR, PPARA, RARA, VDR
nuclear receptor activity [GO:0004879]	6	50	5.71E-07	AR, NR3C1, PGR, PPARA, RARA, VDR
protein binding [GO:0005515]	32	6605	6.98E-07	AR, CASP8, CAT, CCL2, CCND2, CHEK1, CTNNB1, CYBA, CYP3A4, FLT1, GAPDH, GSS, HMOX1, KRT1, KRT8, MDM2, NFE2L2, NOS2, NPPB, NQO1, NR3C1, PGR, PLAT, PPARA, PRDX1, RARA, SMN2, TFRC, TIMP1, TNFRSF1A, TOP2A, VDR
heme binding [GO:0020037]	6	128	2.24E-05	CAT, CYBA, CYP3A4, HBA1, HMOX1, NOS2
transition metal ion binding [GO:0046914]	12	1051	5.27E-05	AR, CYP3A4, HBA1, MDM2, MMP2, MMP7, NR3C1, PGR, PPARA, RARA, TIMP1, VDR
steroid binding [GO:0005496]	5	88	5.87E-05	AR, CYP3A4, NR3C1, PGR, VDR
protein domain specific binding [GO:0019904]	10	706	5.89E-05	AR, CASP8, CHEK1, CTNNB1, CYBA, GAPDH, MDM2, NFE2L2, PPARA, RARA
serine-type endopeptidase activity [GO:0004252]	6	180	7.64E-05	KLK3, MMP2, MMP7, PLAT, PLAU, PROC
Binding [GO:0005488]	38	11878	0.00013	AR, CASP8, CAT, CCL2, CCND2, CD14, CD86, CHEK1, CTNNB1, CYBA, CYP3A4, FLT1, GAPDH, GSS, HBA1, HMOX1, KRT1, KRT8, MDM2, MMP2, MMP7, NFE2L2, NOS2, NPPB, NQO1, NR3C1, PGR, PLAT, PPARA, PRDX1, PROC, RARA, SMN2, TFRC, TIMP1, TNFRSF1A, TOP2A, VDR
zinc ion binding [GO:0008270]	10	800	0.00013	AR, MDM2, MMP2, MMP7, NR3C1, PGR, PPARA, RARA, TIMP1, VDR

Color map | Low | Medium | High

The molecular function analysis was based on the whole genome (*Homo sapiens*) statistical background.

Table 4

Benzalacetophenone derivatives-regulated top 10 cellular components.

Term description [Term ID]	Observed gene count	Background gene count	False discovery rate	Matching proteins in the network
extracellular space [GO:0005615]	14	1134	1.12E-05	CCL2, CD86, FLT1, HBA1, HMOX1, KLK3, MMP2, MMP7, NPPB, PLAT, PLAU, PROC, TIMP1, TNFRSF1A
extracellular region [GO:0005576]	18	2505	8.51E-05	CAT, CCL2, CD14, CD86, FLT1, HBA1, HMOX1, KLK3, KRT1, MMP2, MMP7, NPPB, PLAT, PLAU, PROC, TFRC, TIMP1, TNFRSF1A
intracellular non-membrane-bounded organelle [GO:0043232]	20	4005	0.0034	AR, CASP8, CCND2, CHEK1, CTNNB1, CYBA, FLT1, GAPDH, HBA1, HMOX1, KRT1, KRT8, MDM2, MMP2, NFE2L2, NOS2, NR3C1, RARA, SMN2, TOP2A
cell surface [GO:0009986]	8	690	0.0036	CD14, CD83, MMP7, PLAT, PLAU, RARA, TFRC, TNFRSF1A
cytoplasmic part [GO:0044444]	32	9377	0.0036	AR, CASP8, CAT, CCND2, CD14, CHEK1, CTNNB1, CYBA, CYP3A4, FLT1, GAPDH, GSS, HBA1, HMOX1, KRT1, KRT8, MDM2, MMP2, NFE2L2, NOS2, NQO1, NR3C1, PGR, PLAT, PLAU, PRDX1, PROC, RARA, SMN2, TFRC, TIMP1, TNFRSF1A
protein-containing complex [GO:0032991]	21	4792	0.0066	AR, CASP8, CCND2, CD14, CHEK1, CTNNB1, CYBA, FLT1, GAPDH, HBA1, KLK3, KRT8, MDM2, NFE2L2, NPPB, NR3C1, SMN2, TFRC, TNFRSF1A, TOP2A, VDR
intracellular organelle lumen [GO:0070013]	22	5162	0.0066	AR, CASP8, CAT, CCND2, CHEK1, CTNNB1, HBA1, HMOX1, KRT1, KRT8, MDM2, NFE2L2, NOS2, NR3C1, PGR, PPARA, PROC, RARA, SMN2, TIMP1, TOP2A, VDR
whole membrane [GO:0098805]	11	1554	0.0066	CASP8, CAT, CD14, CTNNB1, CYBA, HMOX1, MDM2, PGR, PLAU, TFRC, TNFRSF1A
Cytosol [GO:0005829]	21	4958	0.0072	AR, CASP8, CAT, CCND2, CHEK1, CTNNB1, GAPDH, GSS, HBA1, HMOX1, KRT1, KRT8, MDM2, NFE2L2, NOS2, NQO1, NR3C1, PGR, PRDX1, RARA, SMN2
Chromatin [GO:0000785]	6	489	0.0082	AR, CCND2, CHEK1, CTNNB1, NFE2L2, RARA

Color map | Low | Medium | High

The cellular components analysis was based on the whole genome (*Homo sapiens*) statistical background.

calculating per residue decomposition energy. The residues *Thr25, Met49, Cys142, Met165, Leu167, Arg188,* and *Gln189* favored the stable complex formation. However, residues *Asn142* and *Glu166* did not favor the interactions. Among these residues, *Met165* showed significant contributions to the binding energy as it had the least contribution energy (−9.12 kJ/mol). However, the contribution energy for other interacting residues varied between −1.42 to −5.601 kJ/mol and also participated in stable complex formation.

Supplementary video related to this article can be found at https://doi.org/10.1016/j.compbiomed.2022.105668.

Table 5

Benzalacetophenone derivatives-regulated top 10 biological processes.

Term description [Term ID]	Observed gene count	Background gene count	False discovery rate	Matching proteins in the network
response to stimulus [GO:0050896]	40	7824	5.09E-12	AR, CASP8, CAT, CCL2, CCND2, CD14, CD83, CD86, CHEK1, CTNNB1, CYBA, CYP3A4, FLT1, GAPDH, GSS, HBA1, HMOX1, KLK3, KRT1, KRT8, MDM2, MMP2, MMP7, NFE2L2, NOS2, NPPB, NQO1, NR3C1, PGR, PLAT, PLAU, PPARA, PRDX1, PROC, RARA, TFRC, TIMP1, TNFRSF1A, TOP2A, VDR
cellular response to chemical stimulus [GO:0070887]	28	2672	5.09E-12	AR, CASP8, CAT, CCL2, CD14, CD86, CTNNB1, CYBA, CYP3A4, FLT1, GAPDH, HBA1, HMOX1, KRT8, MDM2, MMP2, NFE2L2, NOS2, NQO1, NR3C1, PGR, PPARA, PRDX1, RARA, TFRC, TIMP1, TNFRSF1A, VDR
cellular response to stimulus [GO:0051716]	37	6212	6.04E-12	AR, CASP8, CAT, CCL2, CCND2, CD14, CD83, CD86, CHEK1, CTNNB1, CYBA, CYP3A4, FLT1, GAPDH, HBA1, HMOX1, KRT1, KRT8, MDM2, MMP2, MMP7, NFE2L2, NOS2, NPPB, NQO1, NR3C1, PGR, PLAT, PLAU, PPARA, PRDX1, RARA, TFRC, TIMP1, TNFRSF1A, TOP2A, VDR
response to oxygen-containing compound [GO:1901700]	22	1427	6.04E-12	AR, CASP8, CAT, CCL2, CD14, CTNNB1, CYBA, HBA1, HMOX1, KRT8, MDM2, MMP2, NFE2L2, NOS2, NQO1, NR3C1, PPARA, PRDX1, RARA, TIMP1, TNFRSF1A, VDR
cellular response to organic substance [GO:0071310]	24	2219	2.55E-10	AR, CASP8, CAT, CCL2, CD14, CD86, CTNNB1, CYBA, FLT1, GAPDH, HMOX1, KRT8, MDM2, MMP2, NFE2L2, NOS2, NR3C1, PGR, PPARA, RARA, TFRC, TIMP1, TNFRSF1A, VDR
response to abiotic stimulus [GO:0009628]	18	1052	4.16E-10	CASP8, CAT, CCND2, CD14, CHEK1, CYBA, HMOX1, KRT8, MDM2, MMP2, MMP7, NFE2L2, NOS2, NQO1, PLAT, PLAU, PPARA, TNFRSF1A
response to organic substance [GO:0010033]	26	2815	4.16E-10	AR, CASP8, CAT, CCL2, CD14, CD83, CD86, CTNNB1, CYBA, FLT1, GAPDH, HMOX1, KRT8, MDM2, MMP2, NFE2L2, NOS2, NQO1, NR3C1, PGR, PPARA, RARA, TFRC, TIMP1, TNFRSF1A, VDR
response to external stimulus [GO:0009605]	22	1857	4.64E-10	CASP8, CAT, CCL2, CD14, CHEK1, CYBA, FLT1, GAPDH, HMOX1, KLK3, KRT8, MDM2, MMP7, NFE2L2, NOS2, NPPB, NQO1, PLAU, PPARA, RARA, TNFRSF1A, VDR
response to chemical [GO:0042221]	30	4153	5.07E-10	AR, CASP8, CAT, CCL2, CD14, CD83, CD86, CTNNB1, CYBA, CYP3A4, FLT1, GAPDH, HBA1, HMOX1, KRT8, MDM2, MMP2, NFE2L2, NOS2, NQO1, NR3C1, PGR, PLAU, PPARA, PRDX1, RARA, TFRC, TIMP1, TNFRSF1A, VDR
response to stress [GO:0006950]	27	3267	8.84E-10	CASP8, CAT, CCL2, CD14, CD83, CHEK1, CYBA, GAPDH, GSS, HBA1, HMOX1, KLK3, KRT1, KRT8, MDM2, MMP2, NFE2L2, NOS2, NQO1, PLAT, PLAU, PPARA, PRDX1, PROC, TIMP1, TNFRSF1A, TOP2A

Color map	Low	Medium	High

The biological processes analysis was based on the whole genome (*Homo sapiens*) statistical background.

3.7.3. Stability of PL^pro - 4-hydroxycordoin (c30) complex

The PL^pro–4-hydroxycordoin (*c30*) complex showed stable dynamics and a similar trend throughout 150 ns. The RMSD value was stable up to ~80 ns from ~1.2 to ~1.5 Å and ~1.8 to ~2.2 Å for backbone and complex, respectively. After ~80 ns, the RMSD was found to be relatively higher (~1.5–2.3 Å and ~2.2 to 3.5 Å, respectively) due to the increased surface area of protein. The residual fluctuations plotted for the Cα revealed the formation of stable non-bonded contacts in residues with fewer fluctuations observed in 4-hydroxycordoin (*c30*) i.e. *Val203*, *Met207*, *Tyr208*, *Met209*, *Ile223*, *Pro224*, and *Pro248* compared to other non-interacting residues. The Rg value showed stable complex formation during the MD simulation by forming a compact globular shape as revealed by a steady decrease in the Rg value. The supplementary movie (S3) presents the binding mode of 4-hydroxycordoin (*c30*) with PL^pro. It was observed that the loop formed by residues between two sheets was close to the binding pocket and possessed maximum contact with the molecule. However, due to the flexible nature of this loop, it showed the opening of the binding pocket resulting in the increased SASA and ligand movement during the MD simulation after ~85 ns. The initial and final surface area occupied by PL^pro and 4-hydroxycordoin (*c30*) docked complex was 169.50 nm² and 170.29 nm² respectively. The average

surface area occupied by the complex was 170 nm². The complex formed a 3 *H*-bonds of which 2 were consistent. The binding affinity of the 4-hydroxycordoin (*c30*) with PL^pro was estimated by calculating relative binding energy. The complex showed binding energy of −16.28 kcal/mol. To gain more structural insights into the contribution of individual residues in the binding energy, the residue decomposition energy was analyzed. It was observed that 7 residues significantly contributed to the stable complex formation and favored the existing non-bonded interactions i.e. *Val203, Met207, Tyr208, Met209, Ile223, Pro224*, and *Pro248* (Fig. 11). Most importantly, the residues *Tyr208, Met209, Ile223*, and *Pro224* showed significant contributions to the binding affinity by scoring the lowest contribution energy of −2.97, −3.89, −3.82, and −2.91 kJ/mol, respectively.

Supplementary video related to this article can be found at https://doi.org/10.1016/j.compbiomed.2022.105668.

3.7.4. Stability of PL^pro-GRL-0617 complex

The PL^pro-GRL-0617 complex was stable and exhibited similar RMSD values up to 120 ns. The RMSD value for the backbone ranged from ~1.3 Å to ~3.0 Å and ~1.8 Å to ~4.5 Å for the complex. The steady decrease in the backbone RMSD value was observed after ~120 ns (from
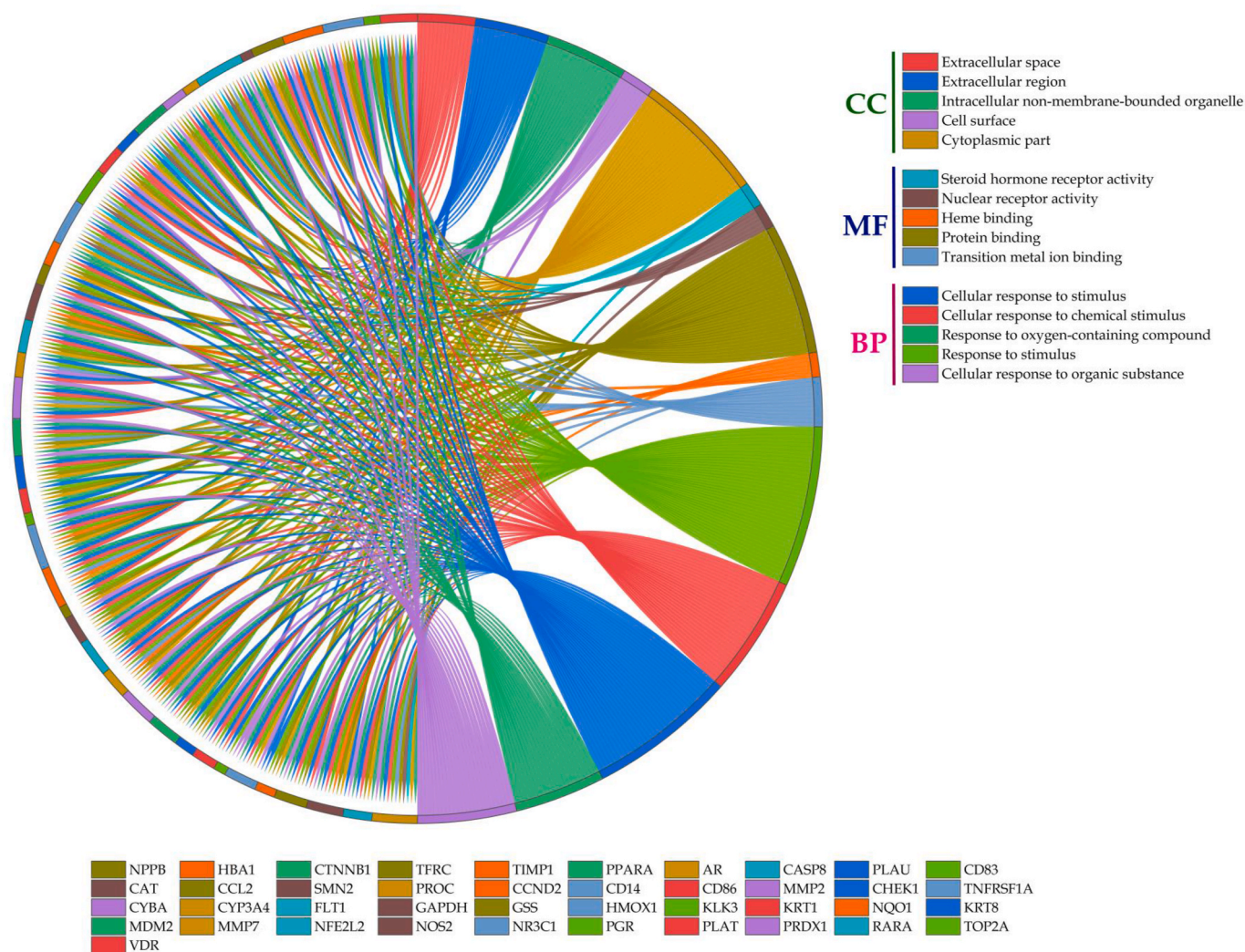
Fig. 5. GO analyses of regulated proteins by benzalacetophenone derivatives presenting cellular components, molecular function and biological processes.

~3.0 Å to 2.0 Å) and remained stable throughout the MD simulation period (150 ns). Similarly, the complex RMSD value showed a similar steady decrease in the RMSD value ranging from ~4.5 Å to ~3.0 Å. After ~120 ns, the RMSD value further increased up to 3.8 Å till 150 ns. The residual fluctuations of *Gly164, Asp165, Thr211, Leu212, Asn216, Ile223, Ala247, Pro248,* and *Tyr265* were relatively less compared to other non-interacting residues. Although *Cys225*, *Val226*, and *Cys227* showed maximum residual fluctuation up to 6 Å due to increased local flexibility, ligand interaction was observed during the simulation. Further, the R*g* value showed the stable complex formation up to ~70 ns. In addition, due to the flexibility of a loop region adjacent to the ligand-binding pocket "*Lys158* to *Val166*", the ligand movement was observed towards other binding pockets (supplementary movie S4) which were also evidenced by an increase in the R*g* value ~70 ns. In addition, GRL-0617 formed the stable non-bonded contacts throughout the 150 ns MD simulation as supported by the stable R*g* pattern. Initially, the SASA showed a flexible binding pocket and increased SASA value. This may have triggered the reorientation of the ligand GRL-0617. The initial and final surface area occupied by PL^{pro} and GRL-0617 docked complex was noted as 164.32 nm^2 and 162.263 nm^2 respectively. The average surface area occupied by the complex was 165.02 nm^2. Similarly, the increased SASA values indicated the binding pocket opening for stable complex formation which was favored mainly due to the flexible nature of the binding pocket residues. The complex formed 4 *H*-bonds of which 2 *H*-bonds were consistent during the simulation period. Further, the PL^{pro}-GRL-0617 complex showed binding energy of −11.83 kcal/mol. In addition, the structural insights into the contribution of individual residues in the binding energy were quantified by calculating the per residue decomposition energy. It was observed that 9 residues had a significant contribution to the stable complex formation and favored the existing non-bonded interactions *i.e. Thr211, Leu212, Asn216, Ile223, Cys225, Val226, Cys227, Ala247,* and *Pro248* (Fig. 12). Most importantly, the residues *Ile223, Cys225, Val226,* and *Cys227* showed significant contributions in the binding affinity by scoring the lowest contribution energy of −0.91, −0.74, −1.86, and −1.08 kJ/mol, respectively.

Supplementary video related to this article can be found at https://doi.org/10.1016/j.compbiomed.2022.105668.

3.7.5. Stability of spike protein - mallotophilippen D (c42) complex

The spike protein-mallotophilippen D (**c42**) complex showed stable dynamics after an equilibration period of 100 ns similar to the other studied complexes. The RMSD value varied between ~1.2 Å to 3 Å and 1.8 Å to ~4 Å for backbone and complex, respectively. The simulation was further extended to 200 ns as this complex reached an equilibration state after 100 ns. The average backbone and complex RMSD values observed were ~2.6 Å and ~3.8 Å, respectively. The residual fluctuations plotted for the Cα, revealed the fewer fluctuations for the residues participating in the non-bonded contacts with mallotophilippen D (**c42**) compared to other non-interacting residues. However, the flexible loop
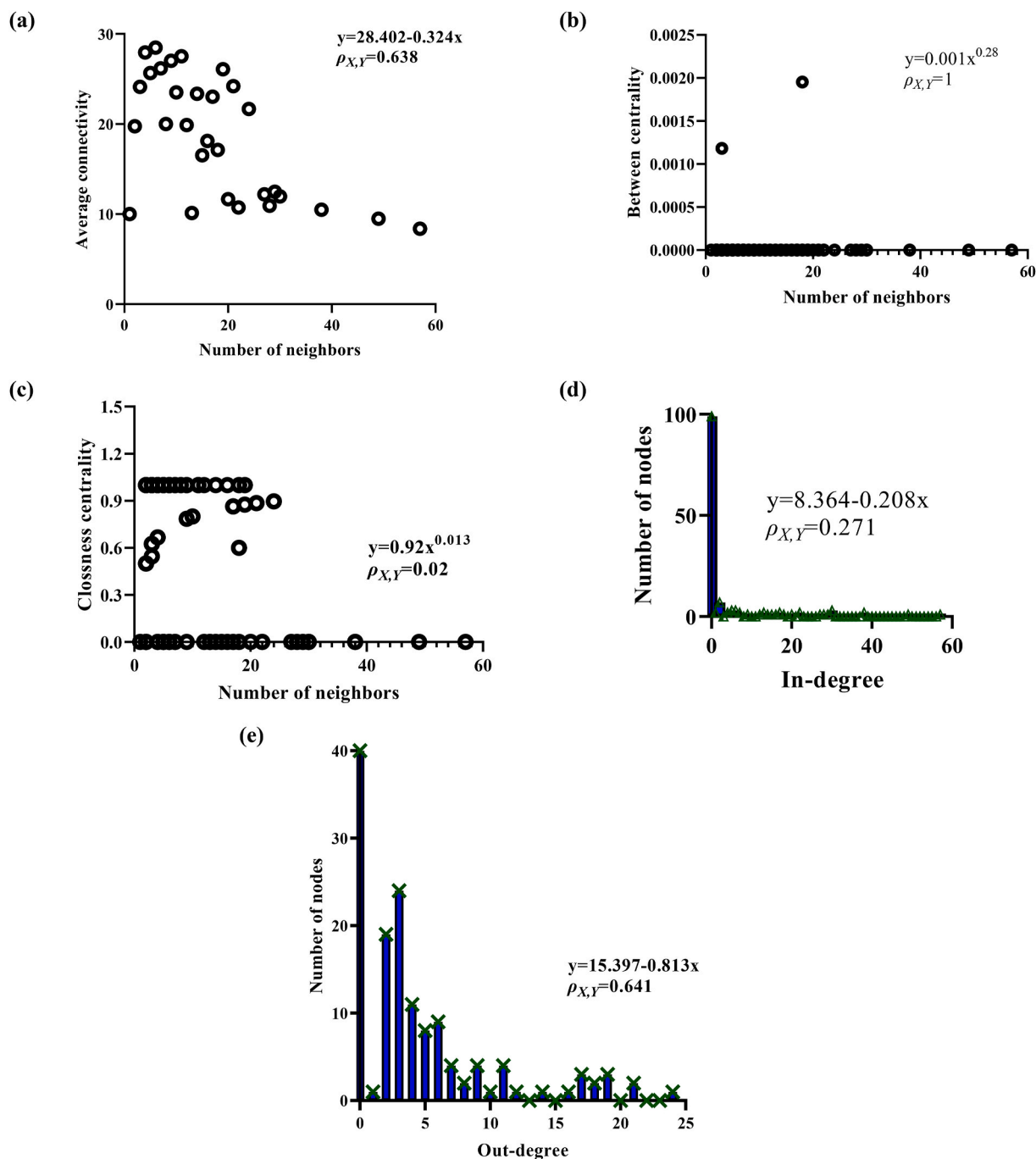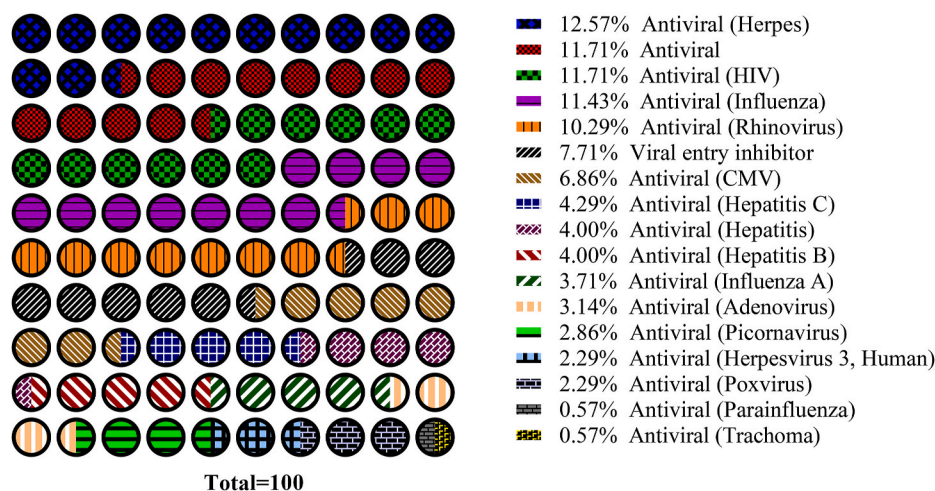
Fig. 6. Relation of number of neighbors with (a) average connectivity, (b) between centrality, and (c) closeness centrality, and (d) in-degree and (e) out-degree with number of nodes.

region formed by residues *Alal344-Trp353* and *Glu516-Thr523* was highly dynamic and showed higher fluctuations (~3 Å). Residues actively engaged in the ligand-protein interactions including *Phe342*, *Leu368*, and *Ile434* showed the least fluctuation (supplementary movie S5). Further, a stable complex was formed during the MD simulation and established a compact globular shape as revealed by a decrease in the Rg value after 10 ns. The complex followed a stable Rg value after 100 ns indicating the proper folding that was required to form a stable complex between ligand and protein. The initial and final surface area occupied by spike protein and mallotophilippen D **(c42)** docked complex was 112.38 nm^2 and 112.6 nm^2 respectively. The average surface area occupied by the complex was 111.4 nm^2. The supplementary movie (S5) demonstrates the detailed binding mode of mallotophilippen D **(c42)**

with spike protein. The complex formed 6 *H*-bonds of which 3 were consistent. The binding affinity of the mallotophilippen D **(c42)** to spike protein was estimated by calculating relative binding energy. In addition, the complex showed binding energy of −34.10 kcal/mol. Further, the per residue contribution energy revealed 12 residues from the binding pocket namely *Phe342*, *Ala363*, *Asp364*, *Tyr365*, *Leu368*, *Leu371*, *Ala372*, *Phe374*, *Ile434*, *Trp436*, *Val511*, and *Leu513* to contribute significantly in the stable complex formation (Fig. 13). The residues *Phe342*, *Leu368*, *Ile434*, and *Trp436* from the binding pocket showed significant contributions to the binding affinity by scoring the least residue decomposition/contribution energy of −5.78, −9.39, −4.71, and −4.20 kJ/mol respectively.

Supplementary video related to this article can be found at https://d

▰▰	12.57% Antiviral (Herpes)
▰▰	11.71% Antiviral
▰▰	11.71% Antiviral (HIV)
▰▰	11.43% Antiviral (Influenza)
▰▰	10.29% Antiviral (Rhinovirus)
▰▰	7.71% Viral entry inhibitor
▰▰	6.86% Antiviral (CMV)
▰▰	4.29% Antiviral (Hepatitis C)
▰▰	4.00% Antiviral (Hepatitis)
▰▰	4.00% Antiviral (Hepatitis B)
▰▰	3.71% Antiviral (Influenza A)
▰▰	3.14% Antiviral (Adenovirus)
▰▰	2.86% Antiviral (Picornavirus)
▰▰	2.29% Antiviral (Herpesvirus 3, Human)
▰▰	2.29% Antiviral (Poxvirus)
▰▰	0.57% Antiviral (Parainfluenza)
▰▰	0.57% Antiviral (Trachoma)

Total=100

Fig. 7. Predicted anti-viral spectra of benzalacetophenone derivatives against multiple viruses. It was predicted that majority of the benzalacetophenone derivatives were active against Herpes virus (12.57%) and least towards Trachoma (0.57%).

oi.org/10.1016/j.compbiomed.2022.105668.

3.7.6. Stability of spike protein - DRI-C23041 complex

The spike protein-DRI-C23041 complex also showed stable dynamics after an equilibration period of 100 ns similar to the spike protein-mallotophilippen D (*c42*) complex. Initially, the backbone and complex RMSD values gradually increased from ~1.8 Å to 5 Å and ~2 Å to ~5.1 Å for backbone and complex respectively. The residues *Val367, Leu368, Asp339, Asp364, Asp389,* and *Leu441* showed relatively fewer fluctuations (~4.0 Å) as they participate in stable non-bonded interactions with DRI-C23041. The flexible loop formed by the residues *Ala475* to *Asn487* showed maximum residual fluctuations (~11.0 Å). In addition, a stable complex was formed by a steady Rg value of ~18 Å. In addition, the anticlockwise rotation of the ligand was observed at about ~63 ns upon the partial unfolding of the complexes which was also evidenced by the increased Rg value to 19.5 Å (supplementary movie S6). However, the ligand regained its original position and occupied stable conformations and the complex formed compact globular shapes as supported by a decrease in the Rg value to 18.3 Å. This structural transition of ligand favored the stable complex formation during the 150 ns MD simulation. The initial and final surface area occupied by spike protein and DRI-C23041 docked complex was 109.379 nm^2 and 107.334 nm^2. The average surface area occupied by the complex was 110.57 nm^2. The complex formed 4 *H*-bonds of which 2 were consistent. The relative binding energy between DRI-C23041 to spike protein was found to be −3.10 kcal/mol. The per residue contribution energy revealed 11 residues from the binding pocket namely *Asp339, Glu340, Asp364, Asp389, Asp398, Asp405, Glu406, Asp427, Asp428, Asp442,* and *Glu516* to contribute significantly in forming the stable complex (Fig. 14) and these residues scored the least per residue decomposition/contribution energy that varied from −11.90 kJ/mol to −27.17 kJ/mol respectively.

Supplementary video related to this article can be found at https://doi.org/10.1016/j.compbiomed.2022.105668.

3.7.7. Principal component and dynamic cross-correlation matrix

We performed principal component analysis to explore the conformational flexibility and diversity of conformations that emerge out from the stable trajectory obtained from 150 ns MD simulations *i.e.* 100–150 ns for five complexes and 150–200 ns for spike protein-mallotophilippen D complex. The maximum collective motion is captured by the first 10 eigenvectors/principal components. Therefore, we precisely studied the first two eigenvectors/PCs (Principal components) in detail. Fig. 15 represents the 2D projection of the first two eigenvectors. It was

observed that standard molecules used in the present study namely Carmofur, GRL-0617, and DRI-C23041, targeting 3CL^{pro}, PL^{pro}, and spike protein, respectively showed larger diversity of conformations during the simulations (shown as a red line in Fig. 15A–C) However, selected ligands namely 3'-(3-methyl-2-butenyl)-4'-O-β-D-glucopyranosyl-4,2'-dihydroxychalcone, 4-hydroxycordoin, and mallotophilippen D targeting 3CL^{pro}, PL^{pro}, and spike protein, respectively showed less diversity of conformations during simulation. This reveals that complexes 3'-(3-methyl-2-butenyl)-4'-O-β-D-glucopyranosyl-4,2'-dihydroxychalcone with 3CL^{pro}, 4-hydroxycordoin with PL^{pro} and mallotophilippen D with spike protein are well equilibrated and stabilized during the simulation. In addition, the larger conformational space occupied by the complexes (standard molecules) exhibited higher conformational flexibility with the maximum number of diverse conformations. Interestingly, the compounds 3'-(3-methyl-2-butenyl)-4'-O-β-D-glucopyranosyl-4,2'-dihydroxychalcone, 4-hydroxycordoin, and mallotophilippen D with 3CL^{pro}, PL^{pro}, and spike protein occupied relatively much lesser conformational space compared to their respective controls/standard. Thus, we propose that screened molecules could be more effective than standard drugs (Fig. 15D–F).

The dynamic cross-correlation of Cα atoms observed in complexes gains more structural insights into the collective motion of the ligand-binding domains. Fig. 16 represents the concerted residual motion of the Cα atoms in all the simulated complexes. The diagonal amber-coloured line shows a strong self-correlation of each residue with itself. The amplitude of correlation to anticorrelation is scaled from amber to blue color respectively. In complex 3'-(3-methyl-2-butenyl)-4'-O-β-D-glucopyranosyl-4,2'-dihydroxychalcone-3CL^{pro}, the binding site residues show anticorrelation with the N-terminal domain of the 3CL^{pro}. However, the amplitude of anticorrelation is moderate while complex 3CL^{pro}-carmofur (standard) showed similar anticorrelation with much lesser amplitude. Thus, we propose binding of 3'-(3-methyl-2-butenyl)-4'-O-β-D-glucopyranosyl-4,2'-dihydroxychalcone that would favor the conformational transition and promote the stable complex formation with enhanced non-bonded interactions compared to its standard molecule *i.e.* carmofur. Likewise, another complex 4-hydroxycordoin-PL^{pro} showed a strong correlation between the residues 50–175, however, the same residues in complex with standard drug GRL-0617 bound to PL^{pro} showed relatively weaker cooperative motion. The cooperative motion expressed by the binding pocket residues ranging from 175 to 240 with the N-terminal region revealed the significance of the active site residues in stabilizing the GRL-0617-PL^{pro} complex. The binding pocket correlation was lost in the complex GRL-0617-PL^{pro}. The standard molecule DRI-C23041-spike protein complex showed strong
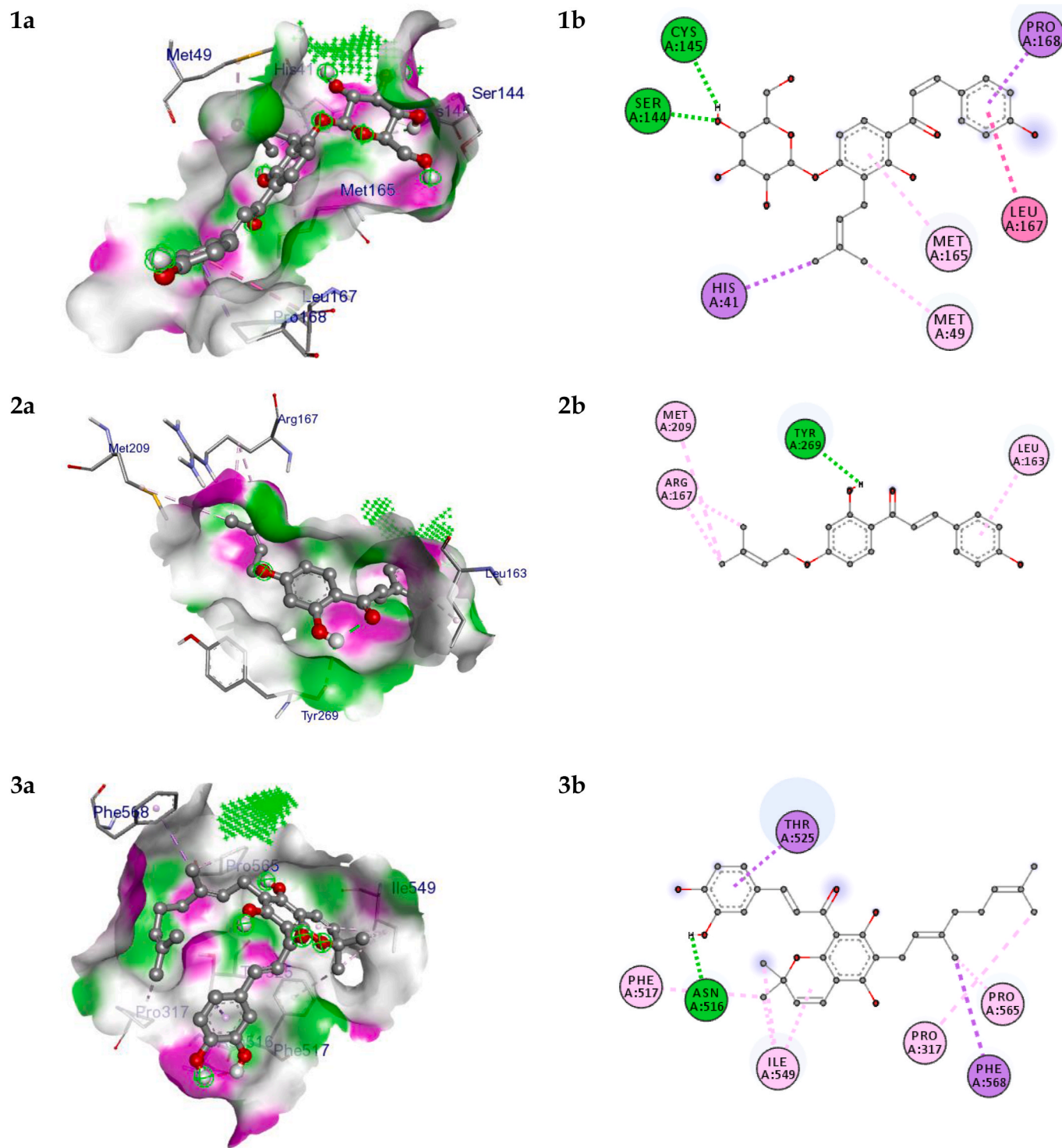
Fig. 8. (a) 3D and (b) 2D interaction of (1) 3'-(3-methyl-2-butenyl)-4'-O-β-ᴅ-glucopyranosyl-4,2'-dihydroxychalcone with 3CL^pro, (2) 4-hydroxycordoin with PL^pro and (3) mallotophilippen D with spike protein RBD. In 3D interaction, ball and stick represents the ligand. The green region on the ligand presents *H*-bond acceptor and pink region presents *H*-bond donor.++++presents active site. All the *H*-bond interactions are presented with green bond whereas hydrophobic interactions are presented other than green color.

cooperative motion for residues 390 to 470 with itself, while these residues in complex spike-mallotophilippen D showed anti-cooperative motion. Moreover, the spike-mallotophilippen D complex showed anti-cooperative motion except for strong self-correlation expressed by all the residues.

Thus, the dynamic cross-correlation matrix showed the cooperative and anti-cooperative motion in the protein highlighting the

conformational flexibility of the studied complexes and stable non-bonded interactions medicated by non-cooperative motion on the opposite side triggered the opening and closing of the binding pocket residues facilitating the stable complex formation during the MD simulation.
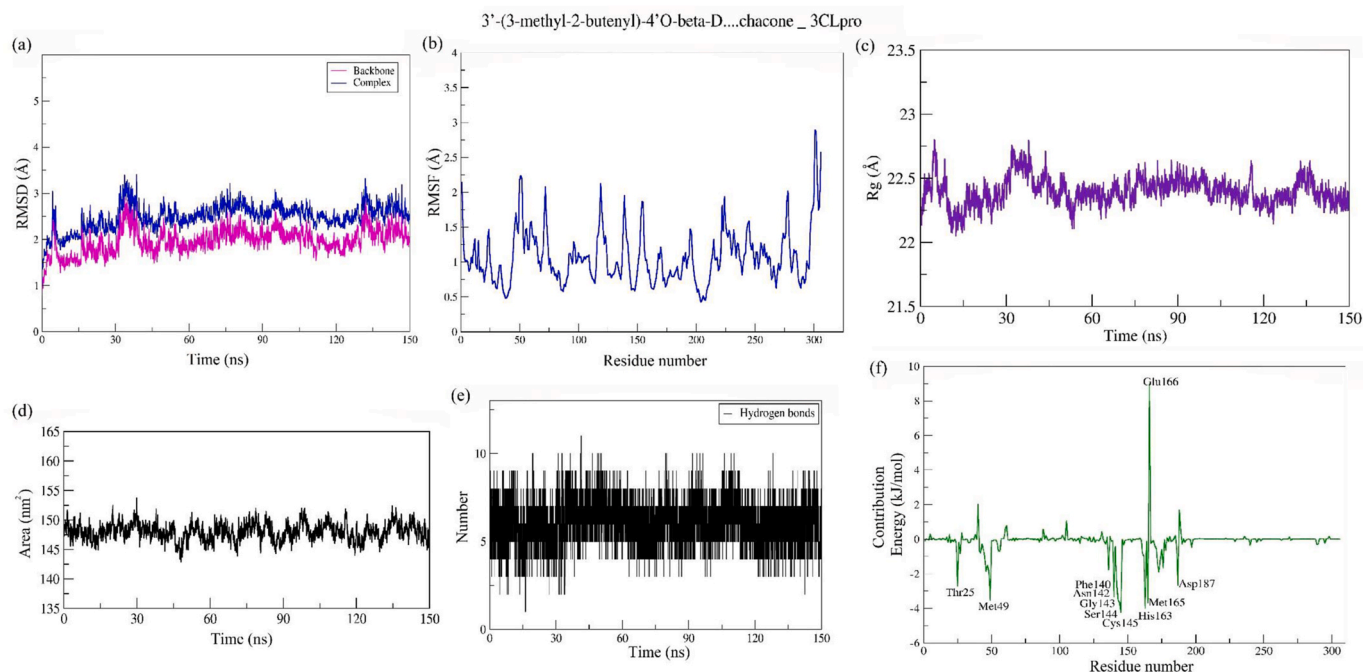
Fig. 9. Parameters describing 3CL^{pro}-3'-(3-methyl-2-butenyl)-4'-O-β-D-glucopyranosyl-4,2'-dihydroxychalcone complex structural stabilities. (a) RMSD of backbone and complex, (b) RMSF, (c) Rg, (d) SASA, (e) number of *H*-bond interactions, and (f) contribution energy plot highlighting the importance of the binding pocket residues in stable complex formation.

Table 6
MM-PBSA calculations of the binding free energy and interaction energies of top hit complexes.

Complex	MM-PBSA (kcal/mol)				
	ΔE_{VDW}	ΔE_{ELE}	ΔG_{Sol}	ΔG_{Surf}	ΔG_{bind}
3CLpro - 13_3'-(3-methyl-2-butenyl)-4'-O-β-D-glucopyranosyl-4,2'-dihydroxychalcone	−52.72 ± 4.33	−29.74 ± 4.04	61.42 ± 4.34	−5.05 ± 0.22	−26.09 ± 3.33
3CLpro-Carmofur	−31.68 ± 2.59	−9.9 ± 1.97	28.46 ± 2.01	−3.49 ± 0.18	−16.67 ± 2.26
PLpro - 18_4-hydroxycordoin	−25.46 ± 5.00	−4.11 ± 3.27	16.42 ± 5.93	−3.13 ± 0.48	−16.28 ± 3.29
PLpro - GRL-0617	−19.15 ± 5.97	−6.17 ± 4.008	15.88 ± 6.70	−2.38 ± 0.66	−11.83 ± 4.57
Spike RBD - mallotophilippen D	−45.84 ± 6.93	−4.03 ± 6.82	21.07 ± 6.66	−5.30 ± 0.44	−34.10 ± 6.84
Spike RBD - DRI-C23041	−42.10 ± 3.20	−12.44 ± 4.74	56.09 ± 5.91	−4.65 ± 0.22	−3.10 ± 3.54

ΔE_{VDW} = van der Waals contribution; ΔE_{ELE} = electrostatic energy; ΔG_{Sol} = polar solvation free energy; ΔG_{Surf} = solvent-accessible surface area; ΔG_{bind} = Binding free energy.

4. Discussion

It has been indicated that immune boosters could play a chief role in prophylaxis against multiple infectious pandemics including COVID-19 as they are more prevalent in compromised immunity. Previously, the immune boosters' role in dealing with COVID-19 has been explained using cheminformatics and bioinformatics approaches [34]. Similarly, the present work attempted to investigate benzalacetophenones (precursors of flavonoids) [35] as immune boosters and anti-viral agents against novel coronavirus.

Initially, the compounds were retrieved and subjected to druglikeness prediction based on the molecular weight, *H*-bond donors, acceptors, and lipophilicity as explained by Lipinski's rule of five. Here, the

majority of the benzalacetophenones were identified with positive druglikeness scores suggesting their oral bioavailability [16]. In addition, few modifications can be made in the structure of benzalacetophenones with negative druglikeness scores to enhance their oral bioavailability. However, it is to be noted that their biological function should not be affected. Further, the top 5 ligands with positive druglikeness scores *i.e.* abyssinone VI (*c1*), isobavachalcone (*c11*), 4-hydroxycordoin (*c30*), mallotophilippen E (*c31*), and oxygenated xanthohumol (*c39*) were predicted for their lipophilicity, water-solubility, pharmacokinetics, and druglikeness as these are central constraints to be considered for the drug action. Interestingly, none of these 5 hits violated Lipkinski (molecular weight <500, number of *H*-bond acceptors <10, number of *H*-bond donors <5, and XLogP<5) [36] and Veber (number of rotatable bonds ≤10, and the total polar surface area ≤140, also questions 500 molecular weight cutoff in Lipinski rule of 5) [37] rules.

In addition, a total of 55 different pathways were regulated by the benzalacetophenones under investigations in which hypoxia-inducible factor (*HIF*)-1, p53, nuclear factor kappa B (*NF-kB*), toll-like receptor, tumor necrosis factor (*TNF*), forkhead box, sub-group O (*FoxO*), estrogen, *Wnt*, *NOD*-like receptor, and interleukin-17 (*IL*-17) signaling pathway and cytokine-cytokine receptor interaction were identified to be concerned in regulating the immune. It has been reported that the *HIF* expression and stabilization are triggered by hypoxia and microbes-associated pathogenesis. Further, *HIF* regulates the host immune function, boosting phagocyte microbicidal capacity and differentiation of T cells followed by a cytotoxic activity. In addition, the *HIF* signaling pathway plays a prime role in inflammation, macrophage metabolism and polarization, microbial infection (both viral and bacterial), antigen presentation, and innate immunity [38]. Similarly, the *HIF*-1 signaling pathway (*hsa04066*) was identified to be regulated *via* the modulation of *FLT1*, *GAPDH*, *HMOX1*, *NOS2*, *TFRC*, and *TIMP1* genes which would play an important role in manipulating the immune system in coronavirus infections and deal with the inflammation in the affected tissue. Also, the *p53* signaling pathway manipulates the immune response *via* the transactivation of key regulators of immune signaling pathways.
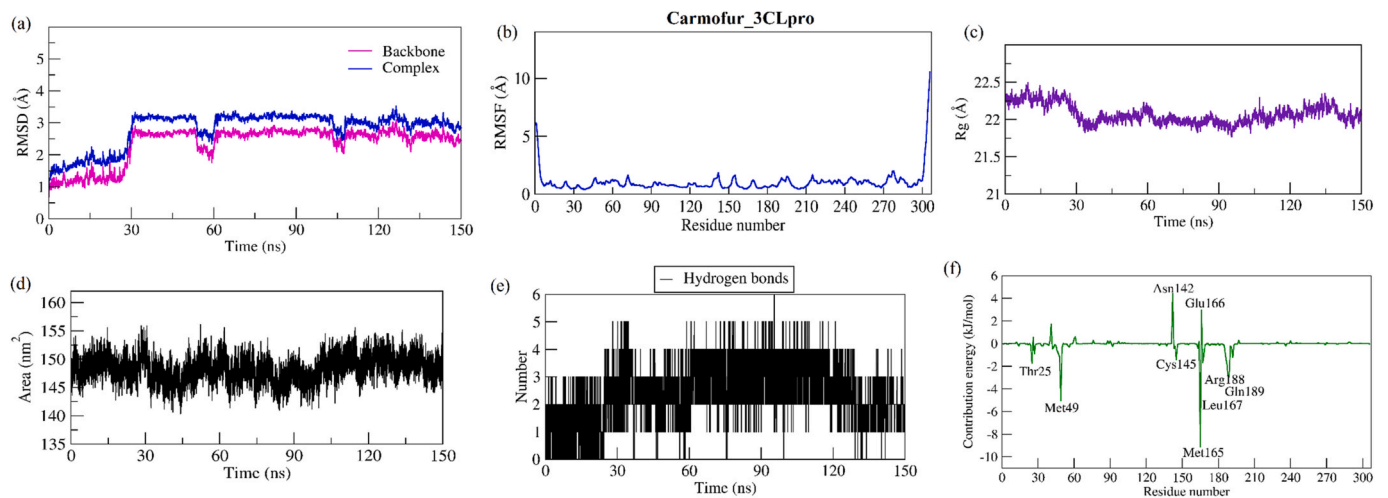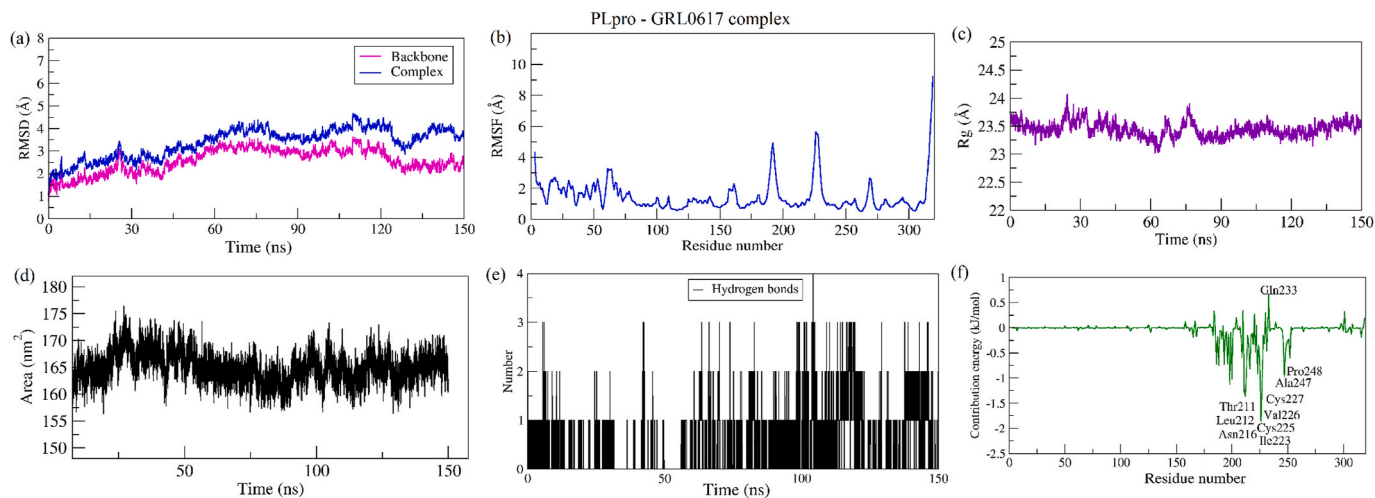
Fig. 10. Parameters describing 3CL^{pro}-Carmofur complex structural stabilities. (a) RMSD of backbone and complex, (b) RMSF, (c) Rg, (d) SASA, (e) number of *H*-bond interactions, and (f) contribution energy plot highlighting the importance of the binding pocket residues in stable complex formation.
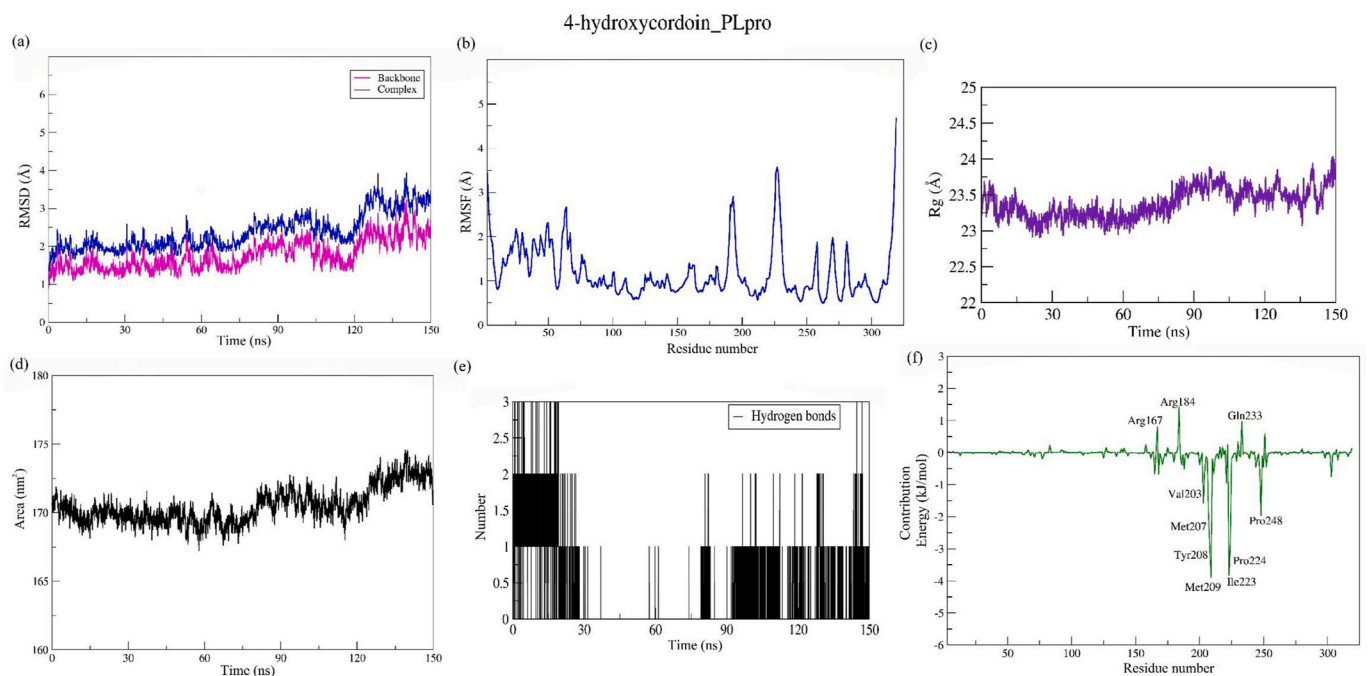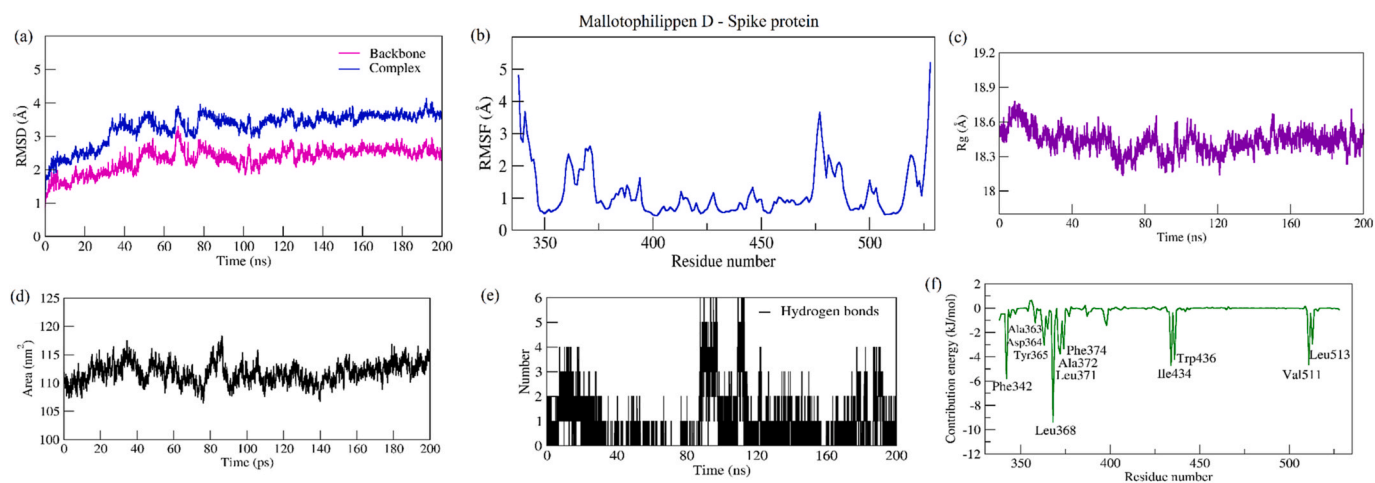

Fig. 11. Parameters describing PL^{pro}-4-hydroxycordoin complex structural stabilities. (a) RMSD of backbone and complex, (b) RMSF, (c) Rg, (d) SASA, (e) number of *H*-bond interactions, and (f) contribution energy plot highlighting the importance of the binding pocket residues in stable complex formation.

Further, multiple genes from the *p53* signaling pathways are also reported in cytokine production, pathogen sensing, inflammation, and clearance of the dead cells [39]. Hence, the benzalacetophenones could be involved in regulating *CASP8*, *CCND2*, *CHEK1*, and *MDM2* genes from the *p53* signaling pathway (*hsa04115*), and may trigger the cytokines to boost the immunity followed by clearance of dead tissues from the body. The inflammatory cytokines like *TNF* or *ILs* influence innate and adaptive immune responses. In addition, their importance has been illustrated by accepting the pathogenesis generated *via* the blockage of single cytokines like *IL*-6 or *TNF* [40]. Herein, benzalacetophenones were also predicated to modulate multiple pathways like *NF*-kB (*hsa04064*), *TNF* (*hsa04668*), and *IL*-17 (*hsa04657*) signaling pathway and cytokine-cytokine receptor interaction (*hsa04060*) which are directly concerned with inflammatory cytokines. Toll-like receptors are usually expressed in sentinel cells (dendritic cells and macrophages) to

recognize microbe-derived structurally conserved molecules and play a key role in the innate immune system. In addition, they recruit specific adaptor molecules, activate transcription factors like *NF-kB*, state the outcome of innate immune responses, and play an important role in multiple aspects of the innate immune response to pathogens [41]. Herein, the benzalacetophenones were identified to regulate the three proteins *i.e. CASP8*, *CD14*, and *CD86* in the toll-like receptor signaling pathway. Further, the *FoxO* subfamily of the forehead (*Fox*) transcription factors play a crucial role in the cell and homeostatic function of immune-relevant cells including T cells, B cells, neutrophils, and other non-lymphoid lineages [42]. Further, benzalacetophenones regulated *FoxO* signaling pathway (*hsa04068*) by modulating three proteins (*CAT*, *CCND2*, and *MDM2*) against 130 background proteins with a false discovery rate of 0.0137. Similarly, estrogen receptors have been acknowledged to develop the immune cells followed by their

Fig. 12. Parameters describing PL^{pro}-GRL-0617 complex structural stabilities. (a) RMSD of backbone and complex, (b) RMSF, (c) Rg, (d) SASA, (e) number of *H*-bond interactions, and (f) contribution energy plot highlighting the importance of the binding pocket residues in stable complex formation.

Fig. 13. Parameters describing spike protein-mallotophilippen D complex structural stabilities. (a) RMSD of backbone and complex, (b) RMSF, (c) Rg, (d) SASA, (e) number of *H*-bond interactions, and (f) contribution energy plot highlighting the importance of the binding pocket residues in stable complex formation.
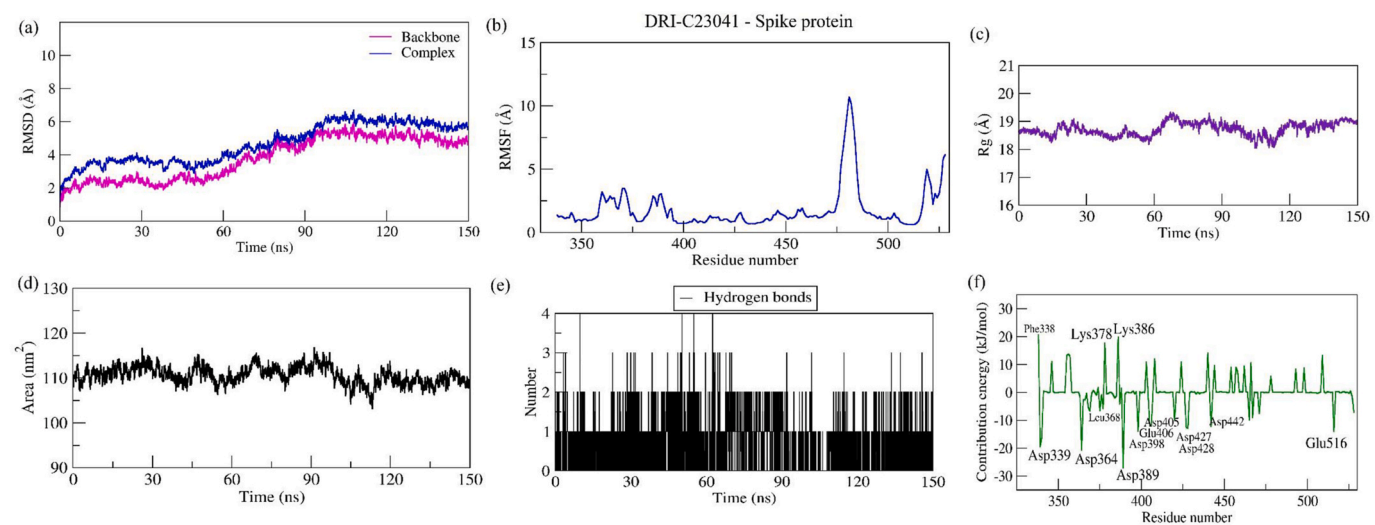
Fig. 14. Parameters describing spike protein-DRI-C23041 complex structural stabilities. (a) RMSD of backbone and complex, (b) RMSF, (c) Rg, (d) SASA, (e) number of *H*-bond interactions, and (f) contribution energy plot highlighting the importance of the binding pocket residues in stable complex formation.
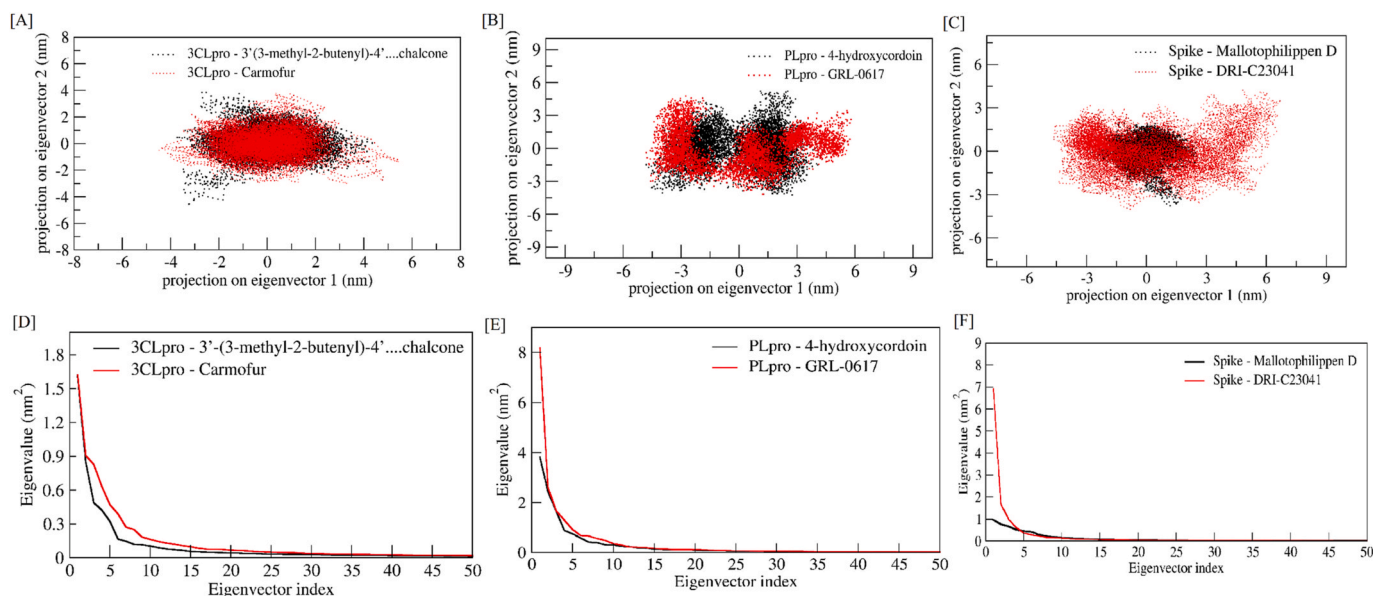
Fig. 15. Principal component analysis of protein-ligand complexes: the collective motion of chalcones (balck) and standard (red) with **(A)** 3CL^{pro}, **(B)** PL^{pro}, and **(C)** spike protein using projections of MD trajectories on two eigenvectors corresponding to the first two principal components. The first 50 eigenvectors were plotted versus eigenvalue for chalcones (balck) and standard molecule (red) with **(D)** 3CL^{pro}, **(E)** PL^{pro}, and **(F)** spike protein.

participation in membrane-initiated steroid signaling. In addition, they produce the type I interferon and also innate cytokine production and develop or function the response of innate immune cells [43]. Likewise, the present work demonstrated benzalacetophenones to regulate the estrogen signaling pathway (*hsa04915*) *via* the modulation of three proteins *i.e. MMP2*, *PGR*, and *RARA* which may trigger the interferons and cytokines production and help in the rapid response of immune cells. Similarly, *Wnt* signal plays an important role in multiple biological processes including immune cell regulation which is very diverse in the natural killer cells development, T-cells initiation, macrophage action on tissue repair, and T-cells thymopoiesis [44]. Herein, benzalacetophenones regulated the *Wnt* signaling pathway (*hsa04310*) *via* the modulation of three proteins *i.e. CCND2*, *CTNNB1*, and *MMP7*, and may contribute to develop and regulate the natural killer cells, T-cells, and macrophages. Similarly, NOD-like receptors function in microbial recognition, and host defense mechanisms are reported and also trigger the host's innate immune response. Additionally, the NOD-like receptor family is concerned with host-pathogen interactions and inflammatory responses [45] which have been regulated *via* the modulation of 3 proteins *i.e. CASP8*, *CCL2*, and *CYBA*.

In the benzalacetophenones-targets-pathways interaction, multiple parameters of the whole network were evaluated. The average connectivity of all the nodes with their neighbors is defined by the "*neighborhood connectivity*" [46]. This variable was defined in the above-mentioned network by neighbors at 63.8%. In addition, "*betweenness centrality*" measures the node frequency to be present on the shortest path between other nodes. This points the node to act as a bridge between the nodes in the network. This helps to identify the shortest path and the frequency of independent nodes to fall on one [47] which was observed to be correlated with neighbors count by 1. Similarly, "*closeness centrality*" tallies each node based on their 'closeness' to other nodes and calculates the shortest path between the nodes. This helps to understand the individual node's influence over the given network most quickly [47]. In the present work, closeness centrality was observed to be dependent on the neighbors by 2%.

During the identification of new antiviral agents for the novel virus, tracing the anti-viral property towards a well-recognized virus could play an easy game. Assuming this, we investigated the benzalacetophenones of interest in the anti-viral biological spectrum. In this, it was observed that selected benzalacetophenones possessed anti-viral

properties against adeno, cytomegalo, hepatitis, herpes, trachoma, influenza, parainfluenza, picorna, pox, rhino, and human immunodeficiency virus. Further, GO analysis also identified the regulation of the infectious disease pathways *i.e.* human papillomavirus infection (*hsa05165*), Kaposi's sarcoma-associated herpesvirus infection (*hsa05167*), viral carcinogenesis (*hsa05203*), HTLV-I infection (*hsa05166*), herpes simplex infection (*hsa05168*), and viral myocarditis (*hsa05416*) that are concerned to viral infection concerning KEGG database. These results further kindled us to investigate the probable anti-viral property of the benzalacetophenones against the novel coronavirus.

To evaluate the probable anti-viral action of benzalacetophenones against SARS-CoV-2, we used the *in silico* molecular docking and all-atom explicit MD simulations to investigate the binding affinity of ligands against 3 targets of novel coronavirus *i.e.* 3CL^{pro}, PL^{pro}, and spike protein receptor-binding domain. Here, all the benzalacetophenones scored binding energy less than −5.0 kcal/mol. Further compounds interacted with all the three targets with a minimum of one *H*-bond interaction except a few *i.e.* 4-chlorochalcone (*c4*), obochalcolactone (*c17*), 4′-O-methylbavachalcone (*c22*), and mallotophilippen E (*c31*) with the 3CL^{pro},2′-hydroxychalcone (*c2*), 4-chlorochalcone (*c4*), 4-hydroxychalcone (*c5*), okanin (*c7*), 2′,3,4,4′,6′-pentahydroxychalcone (*c8*), chalcone (*c10*), (+)-tephrosone (*c12*), pinocembrinchalcone (*c13*), 4′-O-methylbavachalcone (*c22*), and 2′,4′-dihydroxy-6′-methoxy-3′,5′-dimethylchalcone (*c43*) with PL^{pro} and 2′-hydroxychalcone (*c2*), 4-chlorochalcone (*c4*), chalcone (*c10*), desmethylxanthohumol (*c21*), 4′-O-methylbavachalcone (*c22*), 7-methoxypraecansone B (*c29*), mallotophilippen C (*c41*), and 2′,4′-dihydroxy-6′-methoxy-3′,5′-dimethylchalcone (*c43*) with spike protein. In addition, 3CL^{pro} is present in nsp5 that undergoes auto cleavage and releases all downstream replicase subunits to alter the ubiquitin system affecting the functional proteins [48] which were chiefly targeted by obochalcolactone (*c17*) with a −8.5 kcal/mol binding energy however it had no *H*-bond interactions. The viral cycle of coronavirus is regulated by replicase proteins triggered *via* pp1a and pp1ab and is processed by the PL^{pro} [49] which was chiefly modulated by 4-hydroxycordoin (*c30*), and xanthohumol (*c38*) with a binding affinity of −8.2 kcal/mol by both ligands. Likewise, the coronavirus utilizes the ACE2 as a gateway to enter the host cell [50,51] and was majorly targeted by abyssinone VI (*c1*). These results reflect multiple molecules (of a similar category) that
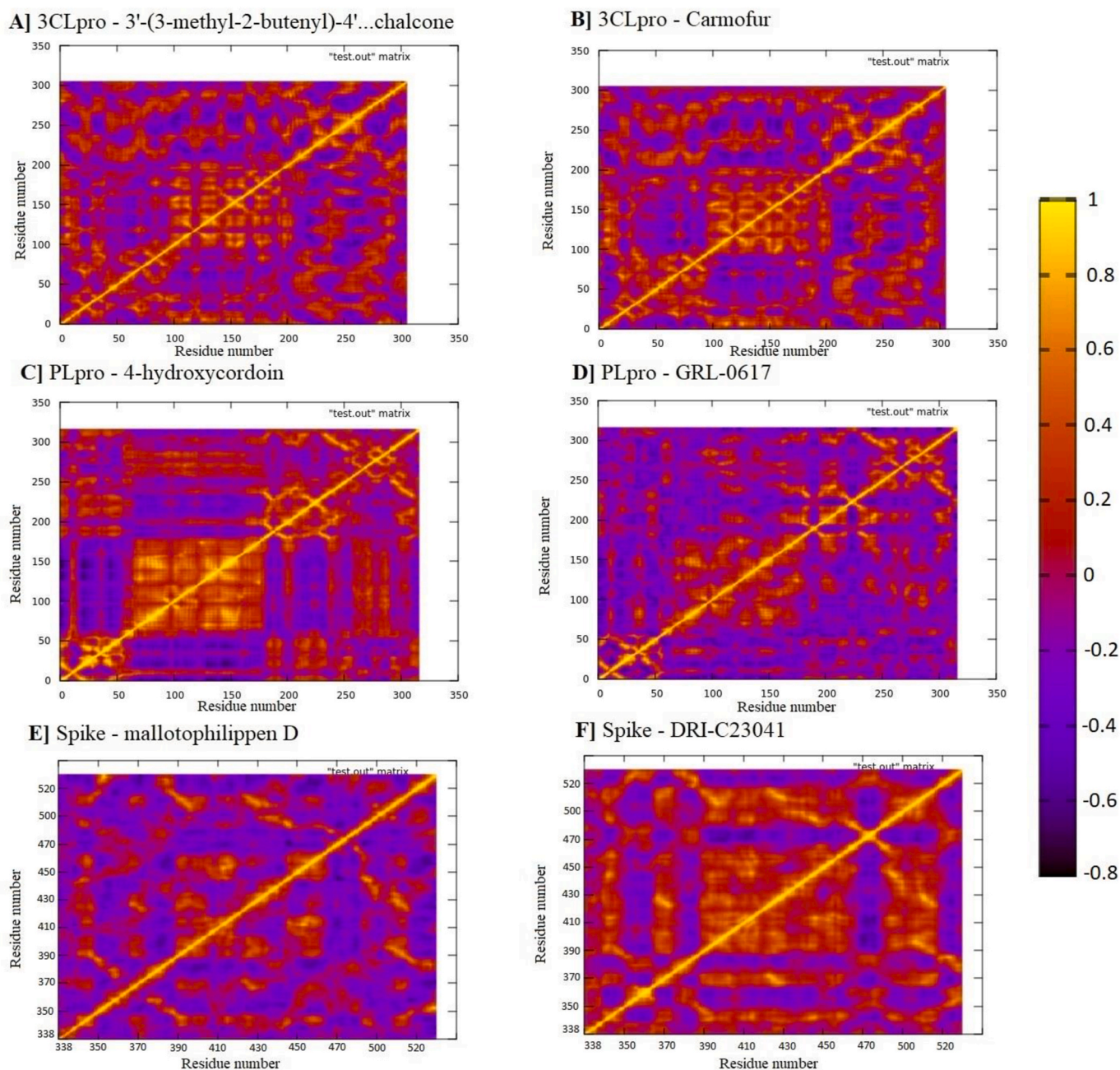
Fig. 16. Dynamic cross-correlation matrix of Cα atoms observed in complexes for benzalacetophenones (A, C, E) and standard drugs (B, D, F) with 3CL^{pro}, PL^{pro}, and spike protein, respectively. The positive regions, which are coloured amber, represent strongly correlated motions of Cα atoms (Cij = 1), whereas the negative regions, which are coloured blue, represent anticorrelated motions (Cij = -1).

may be utilized to target the various sites of virus anatomy due to their affinities towards multiple proteins *via* the "*multi compound(s)-multi protein(s)*" interaction theory. One of the important aspects of the presented study is the identification of viral entry inhibitors which covered 7.71% of total benzalacetophenones under investigation (Fig. 7). Hence, the binding of benzalacetophenones with spike protein receptor-binding domain was added as spike protein and is a direct key to rub the normal cell homeostasis. In addition, one of the important aspects to be considered is that "*right molecule-right target-right duration*" as an irrational assessment may cause tachyphylaxis towards the pathogenesis of interest including COVID-19 which could be solved *via* "*multi component-multi protein*" interaction over "*single compound-single target*" interaction theory. In addition, this study pointed to the regulation of some specific pathways *i.e. TNF*, NF-kB, and *IL*-17 signaling pathways

and cytokine-cytokine receptor interaction (Fig. 17) that are directly concerned with the immune regulation and also manipulate the cytokine storm.

Previously, multiple investigations have been made to implement the homology modeling, molecular docking, MD simulations, and MM-PBSA evaluation to record the drug transport variability, identification of protein allosteric inhibition, the influence of chirality in selective enzyme inhibition, exploring the irrevocable mode of the receptors, and ligand-protein interactions assessment [52–56]. Similarly, in the present work, intermolecular interactions stability of identified potential lead compounds and standard molecules with their respective target were analyzed through classical MD simulation for 150 ns (spike protein - mallotophilippen D (*c42*) complex for 200 ns). Results revealed that 3'-(3-methyl-2-butenyl)-4'-O-β-D-glucopyranosyl-4,
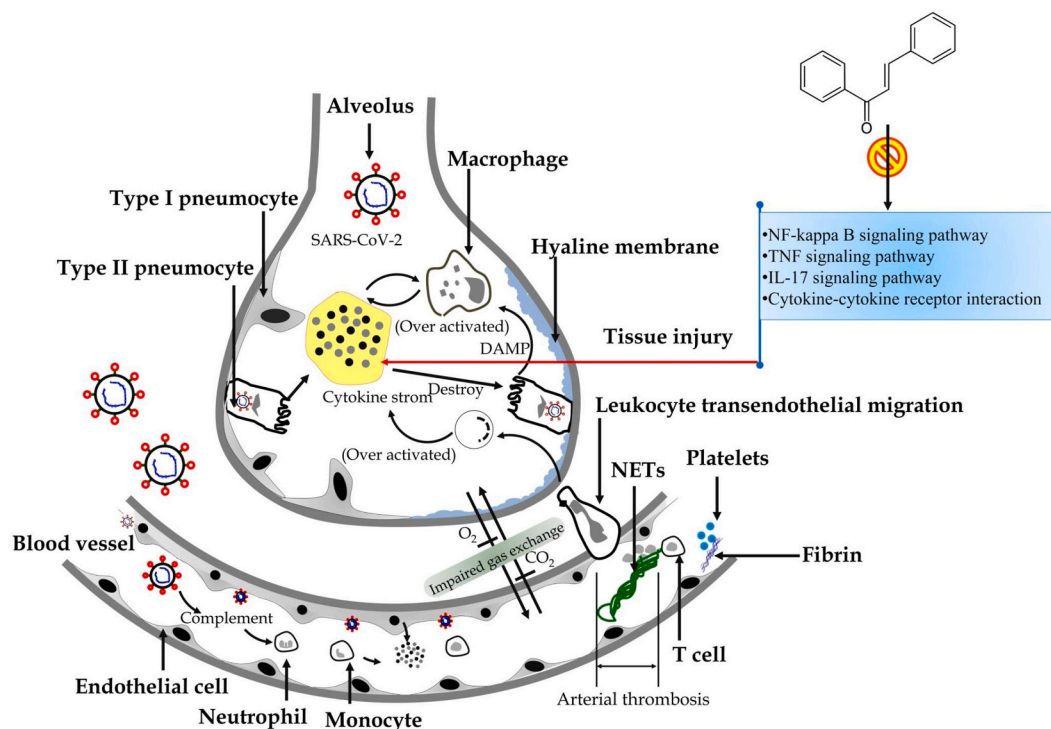
Fig. 17. Benzalacetophenone derivatives in cytokine storm (KEGG entry: *hsa05171*). Benzalacetophenone derivatives were identified to regulate the NF-kB, TNF, IL-17, and cytokine-cytokine receptor interactions.

2′-dihydroxychalcone (**c35**) exhibited stable dynamics with 3CL^pro compared to a standard molecule carmofur. Previously, carmofur was reported to inhibit the coronavirus replication in Vero E6 cells (EC$_{50}$ = 24.30 μM) by interacting with the *Cys145* residue of 3CL^pro [57]. Similarly, in the present study, carmofur was predicted to interact with *Cys145* residue by scoring contribution energy of −1.42 kJ/mol, whereas, 3′-(3-methyl-2-butenyl)-4′-O-β-ᴅ-glucopyranosyl-4,2′-dihydroxychalcone compounds scored −4.24 kJ/mol for *Cys145*. In addition, *Cys145–His41* are the two catalytic dyad residues of 3CL^pro to play an important role in the cleavage of SARS-CoV-2 polyproteins [58]. In addition, other research groups also reported the potential role of targeting *Cys145* to design novel antivirals against 3CL^pro [59,60]. Interestingly, we observed conserved binding site interactions (*Thr25, Met49,* and *Met165*) in both these compounds during the 150 ns MD simulation. Similarly, 4-hydroxycordoin (**c30**) was screened as an inhibitor of PL^pro and formed a stable complex compared to a standard molecule GRL-0617. Previously, GRL-0617 has been reported as a potent PL^pro inhibitor in SARS-CoV-2 infected Vero E6 cells with IC$_{50}$ of 2.1 μM [61, 62]. In the present study, both GRL-0617 and 4-hydroxycordoin (**c30**) formed stable RMSD and shared common interactions with *Ile223* and *Pro248* throughout 150 ns and 200 ns MD production run, respectively, and revealed both as suitable hits as PL^pro inhibitors.

In addition, previously, Bojadzic et al. reported DRI-C23041 to inhibit spike protein RBD domain with IC$_{50}$ of 0.52 μM [63]. In the present study, mallotophilippen D (**c42**) was identified as a spike protein regulator and showed a better binding affinity towards the RBD domain of spike protein compared to a standard molecule DRI-C23041. The MM-PBSA result revealed that the mallotophilippen D (**c42**) possesses the binding free energy of −34.10 kcal/mol, whereas, −3.10 kcal/mol by DRI-C23041 which indicated a higher affinity of mallotophilippen D (**c42**) to spike protein. Further, both DRI-C23041 and mallotophilippenD (**c42**) were found to interact with a common residue *Leu368* of spike protein RBD domain during 150 ns MD simulation. The investigation of complexes for PCA and DCCM also demonstrated that chalcones with 3CL^pro, PL^pro, and spike protein are well equilibrated and stabilized during the simulation *via* occupying relatively much lesser

conformational space and conformational flexibility with a minimum number of diverse conformations compared to standard molecules.

Contemporary, 4-hydroxycordoin (**c30**), a compound with the highest druglikeness score regulated 9 proteins *i.e. FLT1, CD86, CASP8, RARA, KLK3, PLAT, CTNNB1, HMOX1,* and *TOP2A* in which 6 proteins *i. e. CASP8, CTNNB1, TOP2A, CD86, PLAT,* and *HMOX1* were traced to be concerned with the viral infection. *CASP8* encodes caspase 8; a viral pathogen targets the *CASP8*-dependent apoptotic cell and the necrotic cell death pathway that is dependent on the receptor-interacting protein (RIP) 1 and 3. Therefore, acquiring the *CASP8* activity suppresses RIP1 and 3 to strengthen the role in host defense against intracellular viral pathogens [64]. Similarly, CTNNB1 codes catenin β-1 and is responsible for interferon protein synthesis [65] and are the chief modulators of the immune response. In addition, it can interfere with viral infections [66]. Likewise, *TOP2A* codes topoisomerase 2α and its inhibition induces telomeric deoxyribonucleic acid damage and T cell dysfunction during chronic viral infection [67]. Further, *CD86* codes T-lymphocyte activation antigen CD86 and controls antiviral CD8^+ T-Cell function and immune surveillance [68]. *PLAT* codes plasminogen activator and contributes to the deleterious inflammation of the lungs and local fibrin clot formation; may be implicated in host defense against influenza virus infections [69]. Likewise, *HMOX1* codes hemeoxygenase 1. Previously, the SARS-CoV-2 open reading frame 3a protein was reported to bind to the human *HMOX1* protein at high confidence. The *HMOX1* pathway can inhibit platelet aggregation and can have anti-thrombotic and anti-inflammatory properties, amongst others, all of which are critical medical conditions observed in COVID-19 patients [70].

Previously, it has been indicated that genomic RNA of SARS-CoV-2 can manipulate immune genes and deprive their function. In addition, it has been pointed out that genomic RNA could trigger the interleukin interactions and may also trigger the cytokine storm [71]. Also, a study explores the bit part of microRNA (miRNA) in COVID infection to avoid the recognition and attack from the immune response. In an instant SARS-CoV-2 can act as cotton or sponge to absorb the miRNA and force the immune system dysfunction. In addition, it encodes its miRNA, enters the host cell, and is recognized by the host's immune system [72].

Since benzalacetophenones (chalcones) are reported in manipulating the immune response [11], and RNA is concerned with the immune genes synthesis, their probable role in manipulating the genomic RNA interaction host needs to be further investigated.

5. Conclusion

The present study investigated the multiple benzalacetophenones as an immune booster and their anti-viral spectra against SARS-CoV-2. This study reported probable lead antiviral agents namely abyssinone VI (*c1*), isobutrin (*c16*), obochalcolactone (*c17*), 4-hydroxycordoin (*c30*), 3'-(3-methyl-2-butenyl)-4′-O-β-D-glucopyranosyl-4,2′-dihydroxychalcone (*c35*), xanthohumol (*c38*), and 4-mallotophilippen D (*c42*) against COVID-19 by targeting 3CL^pro, PL^pro, and spike protein. In addition, enrichment analysis identified the regulation of various pathways like *HIF*-1, *p53*, *NF-kB*, Toll-like receptor, *TNF*, *FoxO*, estrogen, Wnt, and *IL*-17. Also, *NOD*-like receptors and cytokine-cytokine receptors were triggered that are directly concerned with regulating the immune system and manipulating the cytokine storm. Similarly, there was a triggering of multiple pathways against viral and bacterial infection and endocrine deregulation where the immune system is chiefly compromised. These results suggest the therapeutic option of benzalacetophenone derivative(s) against COVID-19. Limiting to the present findings, we point out that the findings presented in this work are based on processor simulations which need to be further validated with wet-lab experimental protocols.

Ethical statement

This work doesn't include any animal or human studies.

Declaration of competing interest

All the authors of this manuscript declare that they do not have any conflict of interest in any financial and non-financial means. All the authors of this manuscript have read and approved the final draft.

Appendix A. Supplementary data

Supplementary data to this article can be found online at https://doi.org/10.1016/j.compbiomed.2022.105668.

References

[1] A.R. Fehr, S. Perlman, Coronaviruses: an overview of their replication and pathogenesis, Methods Mol. Biol. 1282 (2015) 1–23, https://doi.org/10.1007/978-1-4939-2438-7_1.

[2] Y. Dong, X. Mo, Y. Hu, X. Qi, F. Jiang, Z. Jiang, S. Tong, Epidemiology of COVID-19 among children in China, Pediatrics 145 (2020), e20200702, https://doi.org/10.1542/peds.2020-0702.

[3] C.J. Andersen, K.E. Murphy, M.L. Fernandez, Impact of obesity and metabolic syndrome on immunity, Adv. Nutr. 7 (2016) 66–75, https://doi.org/10.3945/an.115.010207.

[4] S.G. Deeks, B.D. Walker, The immune response to AIDS virus infection: good, bad, or both, J. Clin. Invest. 113 (2004) 808–810, https://doi.org/10.1172/JCI21318.

[5] M. Gendrot, E. Javelle, A. Clerc, H. Savini, B. Pradines, Chloroquine as a prophylactic agent against COVID-19, Int. J. Antimicrob. Agents 55 (2020), 105980, https://doi.org/10.1016/j.ijantimicag.2020.105980.

[6] V. Mody, J. Ho, S. Wills, A. Mawri, L. Lawson, M.C.C.J.C. Ebert, G.M. Fortin, S. Rayalam, S. Taval, Identification of 3-chymotrypsin like protease (3CLPro) inhibitors as potential anti-SARS-CoV-2 agents, Commun Biol 4 (2021) 93, https://doi.org/10.1038/s42003-020-01577-x.

[7] D. Shin, R. Mukherjee, D. Grewe, D. Bojkova, K. Baek, A. Bhattacharya, L. Schulz, M. Widera, A.R. Mehdipour, G. Tascher, P.P. Geurink, A. Wilhelm, G.J. van der Heden van Noort, H. Ovaa, S. Müller, K.P. Knobeloch, K. Rajalingam, B. A. Schulman, J. Cinatl, G. Hummer, S. Ciesek, I. Dikic, Papain-like protease regulates SARS-CoV-2 viral spread and innate immunity, Nature 587 (2020) 657–662, https://doi.org/10.1038/s41586-020-2601-5.

[8] Y. Huang, C. Yang, X.F. Xu, W. Xu, S.W. Liu, Structural and functional properties of SARS-CoV-2 spike protein: potential antivirus drug development for COVID-19, Acta Pharmacol. Sin. 41 (2020) 1141–1149, https://doi.org/10.1038/s41401-020-0485-4.

[9] F. Yazdanpanah, M.R. Hamblin, N. Rezaei, The immune system and COVID-19: friend or foe, Life Sci. 256 (2020), 117900, https://doi.org/10.1016/j.lfs.2020.117900.

[10] Z. Rozmer, P. Perjési, Naturally occurring chalcones and their biological activities, Phytochemistry Rev. 15 (2016) 87–120, https://doi.org/10.1007/s11101-014-9387-8.

[11] J.S. Lee, S.N. Bukhari, N.M. Fauzi, Effects of chalcone derivatives on players of the immune system, Drug Des DevelTher 9 (2015) 4761–4778, https://doi.org/10.2147/DDDT.S86242.

[12] D. Zhou, D. Xie, F. He, B. Song, D. Hu, Antiviral properties and interaction of novel chalcone derivatives containing a purine and benzenesulfonamide moiety, Bioorg. Med. Chem. Lett 28 (2018) 2091–2097, https://doi.org/10.1016/j.bmcl.2018.04.042.

[13] X. Tang, S. Su, M. Chen, J. He, R. Xia, T. Guo, Y. Chen, C. Zhang, J. Wang, W. Xue, Novel chalcone derivatives containing a 1,2,4-triazine moiety: design, synthesis, antibacterial and antiviral activities, RSC Adv. 9 (2019) 6011–6020, https://doi.org/10.1039/C9RA00618D.

[14] Y. Fu, D. Liu, H. Zeng, X. Ren, B. Song, D. Hu, X. Gan, New chalcone derivatives: synthesis, antiviral activity and mechanism of action, RSC Adv. 10 (2020) 24483–24490, https://doi.org/10.1039/D0RA03684F.

[15] A. Lagunin, S. Ivanov, A. Rudik, D. Filimonov, V. Poroikov, DIGEP-Pred: web service for in silico prediction of drug-induced gene expression profiles based on structural formula, Bioinformatics 29 (2013) 2062–2063, https://doi.org/10.1093/bioinformatics/btt322.

[16] C.A. Lipinski, Lead- and drug-like compounds: the rule-of-five revolution, Drug Discov. Today Technol. 1 (2004) 337–341, https://doi.org/10.1016/j.ddtec.2004.11.007.

[17] A. Daina, O. Michielin, V. Zoete, SwissADME: a free web tool to evaluate pharmacokinetics, drug-likeness and medicinal chemistry friendliness of small molecules, Sci. Rep. 7 (2017), 42717, https://doi.org/10.1038/srep42717.

[18] D. Szklarczyk, J.H. Morris, H. Cook, M. Kuhn, S. Wyder, M. Simonovic, A. Santos, N.T. Doncheva, A. Roth, P. Bork, L.J. Jensen, C. von Mering, The STRING database in 2017: quality-controlled protein-protein association networks, made broadly accessible, Nucleic Acids Res. 45 (2017) D362–D368, https://doi.org/10.1093/nar/gkw937.

[19] P. Shannon, A. Markiel, O. Ozier, N.S. Baliga, J.T. Wang, D. Ramage, N. Amin, B. Schwikowski, T. Ideker, Cytoscape: a software environment for integrated models of biomolecular interaction networks, Genome Res. 13 (2003) 2498–2504, https://doi.org/10.1101/gr.1239303.

[20] V.V. Poroikov, D.A. Filimonov, W.D. Ihlenfeldt, T.A. Gloriozova, A.A. Lagunin, Y. V. Borodina, A.V. Stepanchikova, M.C. Nicklaus, PASS biological activity spectrum predictions in the enhanced open NCI database browser, J. Chem. Inf. Comput. Sci. 43 (2003) 228–236, https://doi.org/10.1021/ci020048r.

[21] A.K. Rappé, C.J. Casewit, K.S. Colwell, W.A. Goddard III, W.M. Skiff, UFF, a full periodic table force field for molecular mechanics and molecular dynamics simulations, J. Am. Chem. Soc. 114 (1992) 10024–10035, https://doi.org/10.1021/ja00051a040.

[22] T. Schwede, J. Kopp, N. Guex, M.C. Peitsch, SWISS-MODEL: an automated protein homology-modeling server, Nucleic Acids Res. 31 (2003) 3381–3385, https://doi.org/10.1093/nar/gkg520.

[23] G.M. Morris, R. Huey, W. Lindstrom, M.F. Sanner, R.K. Belew, D.S. Goodsell, A. J. Olson, AutoDock4 and AutoDockTools4: automated docking with selective receptor flexibility, J. Comput. Chem. 30 (2009) 2785–2791, https://doi.org/10.1002/jcc.21256.

[24] DassaultSystèmes Biovia, Discovery S, DassaultSystèmes, San Diego, 2019, 2019, Available at: https://discover.3ds.com/discovery-studio-visualizer-download.

[25] D. Van Der Spoel, E. Lindahl, B. Hess, G. Groenhof, A.E. Mark, H.J. Berendsen, GROMACS: fast, flexible, and free, J. Comput. Chem. 26 (2005) 1701–1718, https://doi.org/10.1002/jcc.20291.

[26] P.S.R. Dwivedi, V.S. Patil, P. Khanal, V.V. Bhandare, S. Gurav, D.R. Harish, B. M. Patil, S. Roy, System biology-based investigation of Silymarin to trace hepatoprotective effect, Comput. Biol. Med. 142 (2022), 105223, https://doi.org/10.1016/j.compbiomed.2022.105223.

[27] R. Kumari, R. Kumar, Open source drug discovery consortium, Lynn A. g_mmpbsa–a GROMACS tool for high-throughput MM-PBSA calculations, J. Chem. Inf. Model. 54 (2014) 1951–1962, https://doi.org/10.1021/ci500020m.

[28] V.V. Bhandare, B.V. Kumbhar, A. Kunwar, Differential binding affinity of tau repeat region R2 with neuronal-specific β-tubulin isotypes, Sci. Rep. 9 (2019), 10795, https://doi.org/10.1038/s41598-019-47249-7.

[29] V.V. Bhandare, A. Ramaswamy, The proteinopathy of D169G and K263E mutants at the RNA Recognition Motif (RRM) domain of tar DNA-binding protein (tdp43)

causing neurological disorders: a computational study, J. Biomol. Struct. Dyn. 36 (2018) 1075–1093, https://doi.org/10.1080/07391102.2017.1310670.

[30] A. Amadei, A.B. Linssen, H.J. Berendsen, Essential dynamics of proteins, Proteins 17 (1993) 412–425, https://doi.org/10.1002/prot.340170408.

[31] A. Amadei, A.B. Linssen, B.L. de Groot, D.M. van Aalten, H.J. Berendsen, An efficient method for sampling the essential subspace of proteins, J. Biomol. Struct. Dyn. 13 (1996) 615–625, https://doi.org/10.1080/07391102.1996.10508874.

[32] H. J D.M. Van Aalten, J.B. Findlay, A. Amadei, H.J. Berendsen, Essential dynamics of the cellular retinol-binding protein-evidence for ligand-induced conformational changes, Protein Eng. 8 (1995) 1129–1135, https://doi.org/10.1093/protein/8.11.1129.

[33] P. Khanal, F. Zargari, B.F. Far, D. Kumar, Y.K. Mahdi, N.K. Jubair, S.K. Saraf, P. Bansal, R. Singh, M. Selvaraja, Y.N. Dey, Integration of system biology tools to investigate huperzine A as an anti-Alzheimer agent, Front. Pharmacol. 12 (2021), 785964, https://doi.org/10.3389/fphar.2021.785964.

[34] P. Khanal, T. Duyu, B.M. Patil, Y.N. Dey, I. Pasha, M. Wanjari, S.S. Gurav, A. Maity, Network pharmacology of AYUSH recommended immune-boosting medicinal plants against COVID-19, J. Ayurveda Integr. Med. 13 (2022), 100374, https://doi.org/10.1016/j.jaim.2020.11.004.

[35] D.N. Dhar, The Chemistry of Chalcones and Related Compounds, Wiley, New York, NY, USA, 1981, p. 285.

[36] C.A. Lipinski, Lead- and drug-like compounds: the rule-of-five revolution, Drug Discov. Today Technol. 1 (2004) 337–341, https://doi.org/10.1016/j.ddtec.2004.11.007.

[37] D.F. Veber, S.R. Johnson, H.Y. Cheng, B.R. Smith, K.W. Ward, K.D. Kopple, Molecular properties that influence the oral bioavailability of drug candidates, J. Med. Chem. 45 (2002) 2615–2623, https://doi.org/10.1021/jm020017n.

[38] A. Palazon, A.W. Goldrath, V. Nizet, R.S. Johnson, HIF transcription factors, inflammation, and immunity, Immunity 41 (2014) 518–528, https://doi.org/10.1016/j.immuni.2014.09.008.

[39] C. Muñoz-Fontela, A. Mandinova, S.A. Aaronson, S.W. Lee, Emerging roles of p53 and other tumour-suppressor genes in immune regulation, Nat. Rev. Immunol. 16 (2016) 741–750, https://doi.org/10.1038/nri.2016.99.

[40] F. Simon, Immunomodulatory cytokines: directing and controlling immune activation, Arthritis Res. Ther. 13 (2011) O14, https://doi.org/10.1186/ar3418.

[41] T. Kawasaki, T. Kawai, Toll-like receptor signaling pathways, Front. Immunol. 5 (2014) 461, https://doi.org/10.3389/fimmu.2014.00461.

[42] S.L. Peng, Foxo in the immune system, Oncogene 27 (2008) 2337–2344, https://doi.org/10.1038/onc.2008.26.

[43] S. Kovats, Estrogen receptors regulate innate immune cells and signaling pathways, Cell. Immunol. 294 (2015) 63–69, https://doi.org/10.1016/j.cellimm.2015.01.018.

[44] M. Haseeb, R.H. Pirzada, Q.U. Ain, S. Choi, Wnt signaling in the regulation of immune cell and cancer therapeutics, Cells 8 (2019) 1380, https://doi.org/10.3390/cells8111380.

[45] L. Franchi, N. Warner, K. Viani, G. Nuñez, Function of Nod-like receptors in microbial recognition and host defense, Immunol. Rev. 227 (2009) 106–128, https://doi.org/10.1111/j.1600-065X.2008.00734.x.

[46] Max planck Institute for informatics, NetworkAnalyzer Online Help. https://med.bioinf.mpi-inf.mpg.de/netanalyzer/help/2.7/#neighborConn, 2018. (Accessed 5 October 2019).

[47] A. Disney, Social network analysis 101: centrality measures explained, Available at: https://cambridge-intelligence.com/keylines-faqs-social-network-analysis/#:%7E:text=Definition%3A%20Betweenness%20centrality%20measures%20the,each%20node%20falls%20on%20one, 2020. (Accessed 27 March 2022).

[48] H.A. Lindner, Deubiquitination in virus infection, Virology 362 (2007) 245–256, https://doi.org/10.1016/j.virol.2006.12.035.

[49] H.A. Lindner, N. Fotouhi-Ardakani, V. Lytvyn, P. Lachance, T. Sulea, R. Ménard, The papain-like protease from the severe acute respiratory syndrome coronavirus is adeubiquitinating enzyme, J. Virol. 79 (2005) 15199–15208, https://doi.org/10.1128/JVI.79.24.15199-15208.2005.

[50] J.H. Kuhn, W. Li, H. Choe, M. Farzan, Angiotensin-converting enzyme 2: a functional receptor for SARS coronavirus, Cell. Mol. Life Sci. 61 (2004) 2738–2743, https://doi.org/10.1007/s00018-004-4242-5.

[51] M. Hoffmann, H. Kleine-Weber, S. Schroeder, N. Krüger, T. Herrler, S. Erichsen, T. S. Schiergens, G. Herrler, N.H. Wu, A. Nitsche, M.A. Müller, C. Drosten, S. Pöhlmann, SARS-CoV-2 cell entry depends on ACE2 and TMPRSS2 and is blocked by a clinically proven protease inhibitor, Cell 181 (2020) 271–280, https://doi.org/10.1016/j.cell.2020.02.052, e8.

[52] T. Fu, F. Li, Y. Zhang, J. Yin, W. Qiu, X. Li, X. Liu, W. Xin, C. Wang, L. Yu, J. Gao, Varidt 2.0: structural variability of drug transporter, Nucleic Acids Res. 50 (2022) D1417–D1431, https://doi.org/10.1093/nar/gkab1013.

[53] W. Xue, T. Fu, S. Deng, F. Yang, J. Yang, F. Zhu, Molecular mechanism for the allosteric inhibition of the human serotonin transporter by antidepressant escitalopram, ACS Chem. Neurosci. 13 (2022) 340–351, https://doi.org/10.1021/acschemneuro.1c00694.

[54] Y. Zhang, J.B. Ying, J.J. Hong, F.C. Li, T.T. Fu, et al., How does chirality determine the selective inhibition of histone deacetylase 6? A lesson from trichostatina enantiomers based on molecular dynamics, ACS Chem. Neurosci. 10 (2019) 2467–2480, https://doi.org/10.1021/acschemneuro.8b00729.

[55] T. Fu, G. Zheng, G. Tu, F. Yang, Y. Chen, X. Yao, X. Li, W. Xue, F. Zhu, Exploring the binding mechanism of metabotropic glutamate receptor 5 negative allosteric modulators in clinical trials by molecular dynamics simulations, ACS Chem. Neurosci. 9 (2018) 1492–1502, https://doi.org/10.1021/acschemneuro.8b00059.

[56] W. Xue, P. Wang, G. Tu, F. Yang, G. Zheng, X. Li, et al., Computational identification of the binding mechanism of a triple reuptake inhibitor amitifadine

[57] Z. Jin, Y. Zhao, Y. Sun, et al., Structural basis for the inhibition of SARS-CoV-2 main protease by antineoplastic drug carmofur, Nat. Struct. Mol. Biol. 27 (2020) 529–532, https://doi.org/10.1038/s41594-020-0440-6.

for the treatment of major depressive disorder, Phys. Chem. Chem. Phys. 20 (2018) 6606–6616, https://doi.org/10.1039/c7cp07869b.

[58] J.C. Ferreira, S. Fadl, A.J. Villanueva, W.M. Rabeh, Catalytic dyad residues His41 and Cys145 impact the catalytic activity and overall conformational fold of the main SARS-CoV-2 protease 3-chymotrypsin-like protease, Front. Chem. 9 (2021) 692168, https://doi.org/10.3389/fchem.2021.692168.

[59] S. Rajpoot, M. Alagumuthu, M.S. Baig, Dual targeting of 3CLpro and PLpro of SARS-CoV-2: a novel structure-based design approach to treat COVID-19, CRSB 3 (2021) 9–18, https://doi.org/10.1016/j.crstbi.2020.12.001.

[60] E.J. Niesor, G. Boivin, E. Rhéaume, R. Shi, V. Lavoie, N. Goyette, M.E. Picard, A. Perez, F. Laghrissi-Thode, J.C. Tardif, Inhibition of the 3CL protease and SARS-CoV-2 replication by dalcetrapib, ACS Omega 6 (2021) 16584–16591, https://doi.org/10.1021/acsomega.1c01797.

[61] Z. Fu, B. Huang, J. Tang, S. Liu, M. Liu, et al., The complex structure of GRL0617 and SARS-CoV-2 PLpro reveals a hot spot for antiviral drug discovery, Nat. Commun. 12 (2021) 1–2.

[62] P. Rao, R. Patel, A. Shukla, P. Parmar, R.M. Rawal, M. Saraf, D. Goswami, Identifying structural-functional analogue of GRL0617, the only well-established inhibitor for papain-like protease (PLpro) of SARS-CoV2 from the pool of fungal metabolites using docking and molecular dynamics simulation, Mol. Divers. 26 (2022) 309–329, https://doi.org/10.1007/s11030-021-10220-8.

[63] D. Bojadzic, O. Alcazar, J. Chen, S.T. Chuang, J.M. Condor Capcha, L.A. Shehadeh, P. Buchwald, Small-molecule inhibitors of the coronavirus spike: ACE2 protein–protein interaction as blockers of viral attachment and entry for SARS-CoV-2, ACS Infect. Dis. 7 (2021) 1519–1534, https://doi.org/10.1021/acsinfecdis.1c00070.

[64] E.S. Mocarski, J.W. Upton, W.J. Kaiser, Viral infection and the evolution of caspase 8-regulated apoptotic and necrotic death pathways, Nat. Rev. Immunol. 12 (2011) 79–88, https://doi.org/10.1038/nri3131.

[65] A. Hillesheim, C. Nordhoff, Y. Boergeling, S. Ludwig, V. Wixler, β-catenin promotes the type I IFN synthesis and the IFN-dependent signaling response but is suppressed by influenza A virus-induced RIG-I/NF-κB signalling, Cell Commun. Signal. 12 (2014) 29, https://doi.org/10.1186/1478-811X-12-29.

[66] D.L. Brassard, M.J. Grace, R.W. Bordens, Interferon-α as an immunotherapeutic protein, J. Leukoc. Biol. 71 (2002) 565–581.

[67] X. Dang, S.C. Ogbu, J. Zhao, L.N.T. Nguyen, D. Cao, L.N. Nguyen, S. Khanal, M. Schank, B.K.C. Thakuri, X.Y. Wu, Z.D. Morrison, J. Zhang, Z. Li, M. El Gazzar, S. Ning, L. Wang, Z. Wang, J.P. Moorman, Z.Q. Yao, Inhibition of topoisomerase IIA (Top2α) induces telomeric DNA damage and T cell dysfunction during chronic viral infection, Cell Death Dis. 11 (2020) 196, https://doi.org/10.1038/s41419-020-2395-2.

[68] S. Fuse, J.J. Obar, S. Bellfy, E.K. Leung, W. Zhang, E.J. Usherwood, CD80 and CD86 control antiviral CD8+ T-cell function and immune surveillance of murine gammaherpesvirus 68, J. Virol. 80 (2006) 9159–9170, https://doi.org/10.1128/JVI.00422-06.

[69] F. Berri, G.F. Rimmelzwaan, M. Hanss, E. Albina, M.L. Foucault-Grunenwald, V. B. Lê, S.E. Vogelzang-van Trierum, P. Gil, E. Camerer, D. Martinez, B. Lina, R. Lijnen, P. Carmeliet, B. Riteau, Plasminogen controls inflammation and pathogenesis of influenza virus infections via fibrinolysis, PLoS Pathog. 9 (2013), e1003229, https://doi.org/10.1371/journal.ppat.1003229.

[70] N. Batra, C. De Souza, J. Batra, A.G. Raetz, A.M. Yu, The HMOX1 pathway as a promising target for the treatment and prevention of SARS-CoV-2 of 2019 (COVID-19), Int. J. Mol. Sci. 21 (2020) 6412, https://doi.org/10.3390/ijms21176412.

[71] nS. Zhang, K. Amahong, C. Zhang, F. Li, J. Gao, Y. Qiu, F. Zhu, RNA-RNA interactions between SARS-CoV-2 and host benefit viral development and evolution during COVID-19 infection, Briefings Bioinf. 23 (2022), bbab397, https://doi.org/10.1093/bib/bbab397.

[72] S. Zhang, K. Amahong, X. Sun, X. Lian, J. Liu, H. Sun, Y. Lou, F. Zhu, Y. Qiu, The miRNA: a small but powerful RNA for COVID-19, Briefings Bioinf. 22 (2021) 1137–1149, https://doi.org/10.1093/bib/bbab062.

Pukar Khanal has been awarded the gold medal (B. Pharm and M. Pharm) by KLE Academy of Higher Education and Research (KAHER) Belagavi, India for his academic performance. His Ph. D. research focused on proposing the mode of action of the traditional medicines using the system biology approach and correlating its output with experimental evidence (*in vitro*; enzyme inhibition, cell line studies, *ex vivo*; isolated tissue preparation, and *in vivo* pharmacological methods). In addition, he has experience in handling the *Danio rerio* as a preliminary animal model including multiple staining techniques, toxicity studies and metabolic rate assay. Currently, he is associated with NGSM Institute of Pharmaceutical Sciences, Nitte (Deemed to be University) Mangalore India.

Vishal S. Patil is currently working as a Senior Research Fellow at ICMR-National Institute of Traditional Medicine, Belagavi. In 2018, he has qualified Graduate Pharmacy Aptitude Test (GPAT). In 2019, he completed his M. Pharmacy (Pharmacology) and secured the highest CGPA score for the academic year 2017–19. His Ph.D. research is focused on the identification of lead molecules against hepatitis B virus infection. His research mainly emphasizes the treatment of diabetes, and neurodegenerative diseases, and prioritizes viral diseases using computational studies *viz.,* network pharmacology, protein modeling, docking, and dynamics, etc., and using enzymes, cell lines, and *in vivo* animal models.

Prof. Patil is currently affiliated to PRES's Pravara Rural College of Pharmacy Pravaranagar Loni-413736, Maharashtra, India as the Professor and Director. He served the KLE College of Pharmacy Belagavi, and Hubli as a Professor, Principal, and Dean Faculty of Pharmacy, KAHER, Belagavi. He has been awarded with the "Prof. M.L. Khorana Memorial award" for publishing the best research paper in the Indian Journal of Pharmaceutical Sciences. His interest in the research area covers the pathophysiology of insulin resistance-induced endothelial dysfunction and neurodegenerative disease. He is also interested in computational pharmacology and its experimental validation in identifying the multiple secondary metabolites from traditional medicines against various diseases. Further, he is also interested in utilizing *Danio rerio* as a preliminary animal model.

Dr. Bhandare is currently working as Dr. D. S. Kothari postdoctoral fellow at the Department of Microbiology, Shivaji University, Kolhapur, India. He received his bachelor and master degrees in Biotechnology from Shivaji University. Immense interest in engineering forced him to receive another master's degree i.e. M.E. in Biochemical Engineering and Biotechnology. He has also completed a postgraduate diploma in Bioinformatics from the same university. He received his doctorate in Bioinformatics from Pondicherry University, India in November 2017. He has expertise in the field of computational biology and biophysics. His research primarily focuses on structural insights into neurodegenerative diseases, structure-based drug discovery, and mutations in hormonal disorders.

Prof. Gurav, Doctorate in Faculty of Medicine from RTM University Nagpur, India, and currently affiliated as Professor, Goa College of Pharmacy, Goa, India. He is the recipient of the "Senior Research Fellowship" of the Indian Council of Medical Research, New Delhi, India. He is also awarded the "International Travel Fellowship" by the Phytochemical Society of Europe and Asia. He is honored as the best "Professor in Pharmacognosy" by Devang Mehta National Education Foundation, India. His research interests are Ayurveda biology, natural products research, computational biology, and herbal nano delivery.

Prarambh S. R. Dwivedi is currently pursuing his Ph.D. at NGSM Institute of Pharmaceutical Sciences, Mangalore India. His areas of interest are an integration of system biology tools with experimental pharmacology (*in vitro*; enzyme inhibition and cell lines and *in vivo*) to decode the mechanism of action of herbal drugs. His research interests focus on diabetes mellitus and breast cancer. His current Ph.D. project aims to propose a possible molecular mechanism of bioactives for the treatment of breast cancer.

Dr. Harish is currently working as Scientist-B at ICMR-National Institute of Traditional Medicine, Belagavi, India. He completed his undergraduate degree in Veterinary Science (BVSc & AH) from Bangalore Veterinary College in 2008. He also received MVSc and Ph.D. degrees from ICAR-Indian Veterinary Research Institute, Izatnagar, India. He has been awarded ICAR-JRF, ICAR-SRF, CSIR-JRF, and ICMR-JRF fellowships. He is interested in the validation and elucidation of the mechanism of action of traditional medicines against prioritized viral diseases.

Prof. Shastry is currently serving the NGSM Institute of Pharmaceutical Sciences, Mangalore as a Professor, Principal, and Dean for the Faculty of Pharmacy, Nitte (Deemed to be University), Mangalore, India. He has received various grants from the Board of Research in Nuclear Sciences (BRNS), Government of India for his extensive research on radio-protective indigenous medicinal plants from the Western Ghats of Karnataka. He has gained interest in utilizing *in-silico* tools to predict possible molecular mechanisms for various folk medicines. In addition, he interests in utilizing various animal models to validate computational findings.

Dr. Roy is Scientist-G and Director, ICMR-National Institute of Traditional Medicine, Belagavi, India. He is a microbiologist and molecular biologist who has worked extensively in public health and at the interfaces of field and laboratory, traditional medicines and modern medicine, research, and policy. Dr. Roy is a University Gold Medallist and the recipient of prestigious awards like Major General Saheb Singh Sokhey Award, Medical Innovation Fund Award ICMR, New Delhi, and Dr. S. S. Misra Memorial Award from NAMS, India.